SJCE
SCIENTIFIC
JOURNAL
OF CIVIL
ENGINEERING

SS CYRIL AND METHODIUS UNIVERSITY
FACULTY OF CIVIL ENGINEERING

ISSN 1857-893X
Volume 11
Issue 2
December 2022

SJCE
SCIENTIFIC
JOURNAL
OF CIVIL
ENGINEERING

SS CYRIL AND METHODIUS UNIVERSITY
FACULTY OF CIVIL ENGINEERING

EDITORIAL - Preface to Volume 11 Issue 2 of the Scientific Journal of Civil Engineering (SJCE)

Vladimir Vitanov EDITOR - IN - CHIEF

Dear Readers,

The **S**cientific **J**ournal of **C**ivil **E**ngineering (SJCE) is an international, peer-reviewed, open-access journal that has been published bi-annually since December 2012. Since December 2021, SJCE has established its own website and implemented a fully digital submission, review, and publication process. For additional information about the online version of the Journal, please visit www.sjce.gf.ukim.edu.mk.

Our commitment at SJCE is to publish and disseminate high-quality and innovative scientific research in the broad field of engineering sciences. The journal is dedicated to advancing technical knowledge and promoting innovative engineering solutions in civil engineering, geotechnics, survey and geo-spatial engineering, environmental protection, construction management, and related areas.

We strive to offer the best platform for researchers to publish their work transparently and integrally through the open-access model, providing a forum for original papers addressing theoretical and practical aspects of civil engineering and related sub-topics.

As the Editor-in-Chief of the Scientific Journal of Civil Engineering, it gives me great pleasure to present to you the Second Issue of Volume 11, an open-subject edition featuring six scientific research papers that have successfully undergone the general review process of this journal.

These papers cover a range of advanced scientific topics. The first paper analyses static pile load testing to determine axial capacity, demonstrating minor deformations and employing numerical modelling for assessment the ultimate axial capacity of the pile. The second explores automatic building footprint extraction from LiDAR data. The third paper introduces a method to determine the rotational stiffness of welded connections between square columns and I-beams, comparing semi-rigid versus fully rigid connections in frame structures. The fourth paper examines challenges in providing displacement overview in composite steel-concrete frames, proposing a numerical solution, and comparing findings with EN 1994-1-1 recommendations. The fifth paper discusses causes of embankment dam failure, emphasizing overtopping as the most common reason, and analyses flood propagation at a cascade system of tailings dams, while the final paper outlines the characteristics of the Transverse Mercator projection and its applications, highlighting its advantages over the Gauss-Kruger projection.

I sincerely hope that the papers published in this issue will inspire further research in these fields. I extend my gratitude to all the authors for contributing to this issue, and I appreciate the detailed and timely evaluations provided by the reviewers. Finally, I wish to extend my heartfelt gratitude to the editorial office members who demonstrated remarkable enthusiasm and made significant contributions to this journal issue.

Best regards,

Vladimir Vitanov

Editor-in-Chief

Scientific Journal of Civil Engineering

December 2022

SJCE
SCIENTIFIC JOURNAL OF CIVIL ENGINEERING

Impressum

FOUNDER AND PUBLISHER

Faculty of Civil Engineering
Partizanski odredi 24, 1000
Skopje, N. Macedonia

PRINT

This Journal is printed in Mar-saz DOOEL Skopje

EDITORIAL OFFICE

Faculty of Civil Engineering
Partizanski odredi 24, 1000
Skopje, N. Macedonia
tel. +389 2 3116 066
fax. +389 2 3118 834
prodekan.nauka@gf.ukim.edu.mk

EDITOR IN CHIEF

Prof. PhD **Vladimir Vitanov**
University "Ss. Cyril and Methodius"
Faculty of Civil Engineering
Partizanski odredi 24, 1000
Skopje, N. Macedonia
v.vitanov@gf.ukim.edu.mk

ISSN: 1857-839X

SJCE
SCIENTIFIC JOURNAL OF CIVIL ENGINEERING

Impressum

ORDERING INFO

SJCE is published bi-annually.
All articles published in the journal have been reviewed.
Edition: 100 copies

SUBSCRIPTIONS

Price of a single copy:
for Macedonia (500 den);
for abroad (10 EUR + shipping cost).

BANKING DETAILS (NORTH MACEDONIA)

Narodna banka na RNM
Account number:
160010421978815
Prihodno konto 723219,
Programa 41

BANKING DETAILS (INTERNATIONAL)

Correspond bank details:
Deutsche Bundesbank Zentrale
Address: Wilhelm Epstein Strasse 14 Frankfurt am Main, Germany
SWIFT BIC: MARK DE FF
Bank details:
National Bank of the RNM
Address: Kompleks banki bb 1000 Skopje North Macedonia
SWIFT BIC:NBRM MK 2X
IBAN: MK 07 1007 0100 0036 254
Name: Gradezen fakultet Skopje

SELECT A PROFESSION

CREATIVE	SOPHISTICATED	RECOGNIZED	RESPONSIBLE
ENDURING	UP-TO-DATE	WORLWIDE	IMPORTANT

WWW.GF.UKIM.EDU.MK

OUR FACULTY CAN GIVE YOU

IMPULSE !	SCHOLARSHIPS FOR THE BEST	ASSURANCE !	COORPERATION WITH INDUSTRY AND INTERNATIONAL UNIVERSITIES
SIMPLE ENROLLMENT	MOTIVATION !	100% EMPLOYMENT AND INTERNATIONALLY RECOGNIZED DIPLOMA	SUPPORT !

WWW.GF.UKIM.EDU.MK

SJCE
SCIENTIFIC JOURNAL OF CIVIL ENGINEERING

CONTENTS

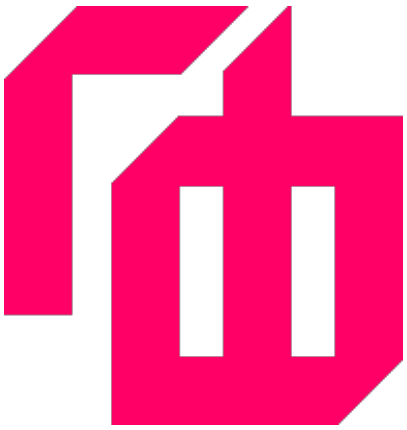

СЕКОГАШ БИДИ ИН

Sead Abazi
PhD, Assistant Professor
University ‘Ss. Cyril and Methodius’
Faculty of Civil Engineering – Skopje
N. Macedonia
sead@gf.ukim.edu.mk

Bojan Susinov
PhD, Assistant Professor
University ‘Ss. Cyril and Methodius’
Faculty of Civil Engineering – Skopje
N. Macedonia
susinov@gf.ukim.edu.mk

Spasen Gjorgjevski
PhD, Full Professor
University ‘Ss. Cyril and Methodius’
Faculty of Civil Engineering – Skopje
N. Macedonia
gjorgjevski@gf.ukim.edu.mk

IN-SITU DETERMINATION AND NUMERICAL MODELLING OF AXIAL CAPACITY OF PILES IN GRAPHITIC SCHISTS

This paper presents the analysis of results of static pile load testing for determining the axial capacity of pile foundation carried out in graphitic schists. While multiple tests have been made on the pile foundations of the viaducts, this paper will only present the process of pile load testing carried out on a single pile, with a length of 16 m and diameter of Ø1200 mm, whereas the analytically estimated load capacity is set to 9 MN. A unique steel platform as reactive system has been designed in order to provide a counter load for the downward forces applied during testing. The results show that the deformations of the pile under the effect of the designed loads are minor in comparison to the allowable ones foreseen in the design. In order to model the ultimate bearing capacity of the pile foundation, numerical modeling has been made by calibrating the model for the loads applied during the test and an assessment of the ultimate axial capacity of the pile.

Keywords: static pile load testing, pile foundations, interaction, axial pile capacity

1. INTRODUCTION

This paper presents the methodology used in determining the pile bearing capacity carried out in graphitic schists on the A2 state highway project (Kichevo – Ohrid). The choice of the constructive system depends mainly on the geotechnical conditions, which are a result of highly complex and long-lasting effects of the geological structure of the terrain, hydrological, hydro-geological conditions, seismicity, the morphology of the terrain and other influences, which in an inherent way affect the stability, deformability and bearing capacity of the substrate. Exceptional attention is channelled towards the analysis of the results from the experimental direct measurements on site, with a uniquely designed reactive steel platform system that acts as a counter load for the downward loads applied. The input parameters for the analysis are different, generally depending on the characteristics of the structure, the load levels, the foundation depths, the parameters of the substrate, the

dimensions of the foundation and other structural characteristics. The entire process includes: analysis of the terrains geological profile, design of a reactive system that is further on used as a counter load during the test, a defined methodology for load application, on site measurements, reporting the results and calibration with numerical modeling.

2. ON SITE CONDITIONS AND DESCRIPTION OF THE STRUCTURE

The structure is a viaduct bridge from the Kichevo – Ohrid highway project, near the village of Lavchani near Kichevo. It was constructed with the balanced cantilever method, with a pile foundation system consisting of 56 piles connected with a pile cap, with dimensions of 23.6 x 31.0 m. Pile no. 16 of pillar P2 (Figure 1), has been chosen as a representative test pile, with a length of 16 m and diameter of Ø1200 mm. The design axial capacity of the pile is 9000 kN.

According to the geotechnical investigations report, as well as the technical report of the pile, the geotechnical profile of the terrain is defined with graphitic schists fractured at surface, filled with clayey material and a thickness of 0.5 m, under which there is a homogeneous medium composed of carbonate-graphitic schists with extremely high strength, up to the investigated depth of 30 m (Figure 2). Figure 3 shows a panoramic view of the construction site, as well as the complex geological and geotechnical conditions in which the construction activities are carried out.

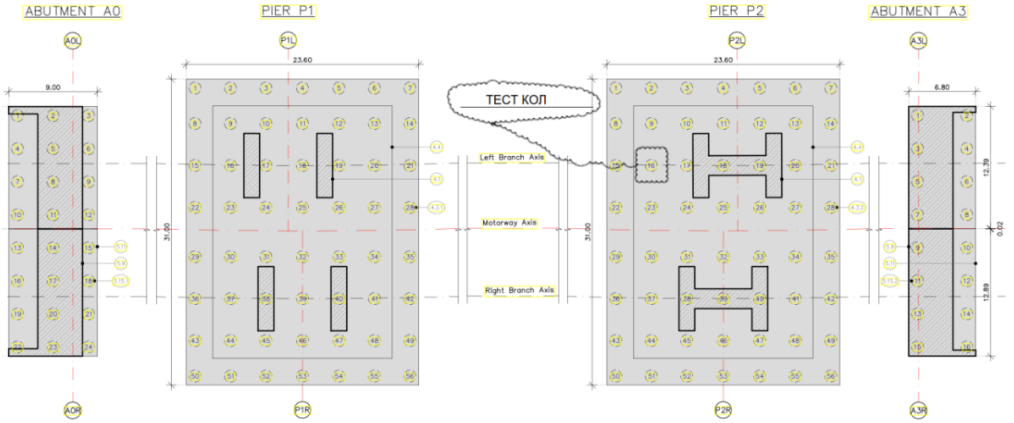

Figure 1. Position of the test pile in pile foundation

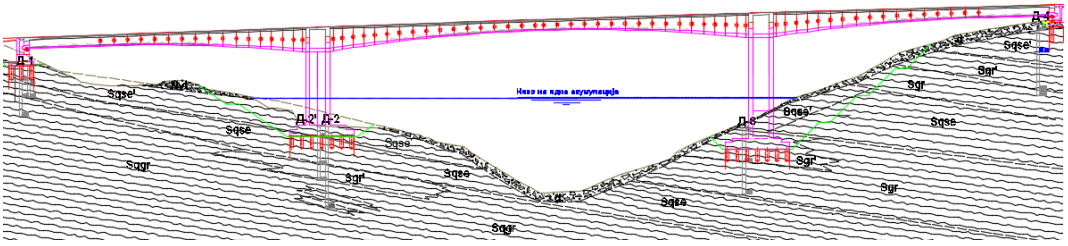

Figure 2. Longitudinal geotechnical profile of the viaduct

Figure 3. Panoramic view of the construction site and geological conditions

3. COUNTER LOAD REACTIVE STEEL PLATFORM

According to the design documentation, the axial pile capacity is 9000 kN. According to the National technical regulations book for the design of foundations, but also the recommendations of EN1997, ASTM and other regulations, it is mandatory to apply the maximum designed load on the test pile. For this purpose, a steel platform of cross beams has been designed that will connect four adjacent anchor piles loaded in tension. This type of structure forms a reactive system with a sufficient capacity to receive the loads with which it is necessary to load the test pile during the test (Figures 4 and 5).

4. METHODOLOGY

The testing procedure is carried out in accordance with the ASTM 1143D/1143M-20 standard. A standard procedure with three levels of loading and unloading was implemented, according to a previously defined Program. The load is applied using a system of 10 hydraulic load cells, with a unit capacity of 1000 kN (or 10 x 1000 = 10,000 kN). In accordance with the practice and standard procedure, the hydraulic cells are carefully placed on a special steel support plate that is positioned on the head of the test pile. The presses are connected with hydraulic hoses with an installed measuring instrument through which the total pressure in the entire load applying system is controlled. Because the hydraulic cells are connected to a single system, through a suitable distributor, when the hydraulic oil is pumped, they simultaneously apply the force on the platform and the cross beam reactive system and thus on the pile itself. Monitoring the test pile settlement under the effect of the applied load is carried out through three digital strain gauges that are place axisimmetrically on the lower special cover plate. The results for the applied load and test pile deformations are monitored with appropriate equipment during the testing.

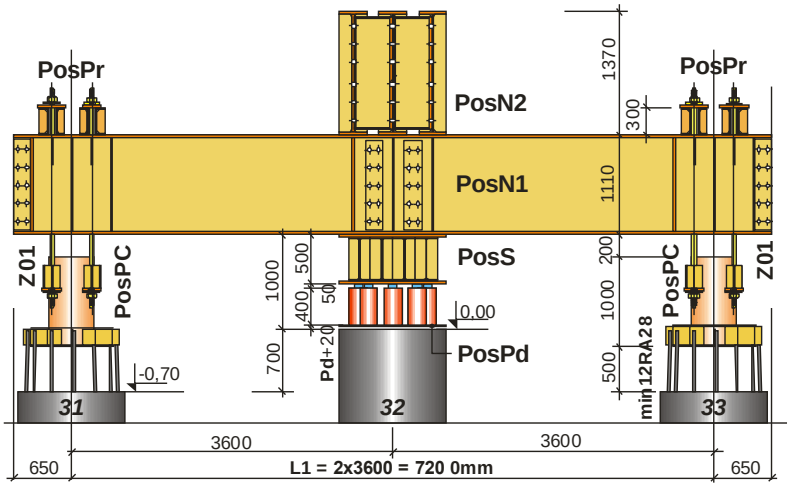

Figure 4. Cross section of the counter load steel platform reactive system

Figure 5. View of the cross beam reactive platform system during testing

5. TEST RESULTS

In accordance with the program, in the first load cycle, the test pile is loaded with a force equal to 50% of the design estimate (4500 kN), with a load application step of 10% (900 kN). The pile deformation criteria must be satisfactory (< 25 mm in the past hour of testing), in order for the test to proceed on to the next step of loading. The unloading down to 900 kN is performed with a 10% load reduction step. The next load increase is set to 6300 kN, followed by a reduction of loading force to 900 kN. The final load is set to 9000 kN and unloading to a load force of 0 kN (Figure 6). The first cycle of loading the test pile to 4500 kN has been reached within 350 min, the second cycle of up to 6300 kN in 560 min and the third cycle of 9000 kN in 880 min. The load – settlement curve is shown in Figure 7. In the first loading cycle, approximately 0.96 mm of settlement is reached, followed by a load decrease with recorded elastic deformation of about 0.40 mm. The second loading cycle is performed to a force of 6300 kN, during which a settlement of 1.27 mm is reached. This implies a settlement increase of 27%, with a loading force increase of 40%. Hence, the trend of increasing deformations and the non-linear character of the material behavior through strengthening can be clearly perceived. After this, the second unloading cycle was applied with plastic deformations of 0.65 mm. In the third and final cycle, there is a deformation of 2.08 mm. This implies that with an increase in loading force of 43%, the deformations, that is, the test piles settlement is increased by 63.8%. Figure 8 presents the time dependence of the settlement, which is still significant in determining the yielding point and the maximum limit deformations of the pile-soil interaction system. The measured maximum settlements of the three loading cycles for the test pile are given in table 1.

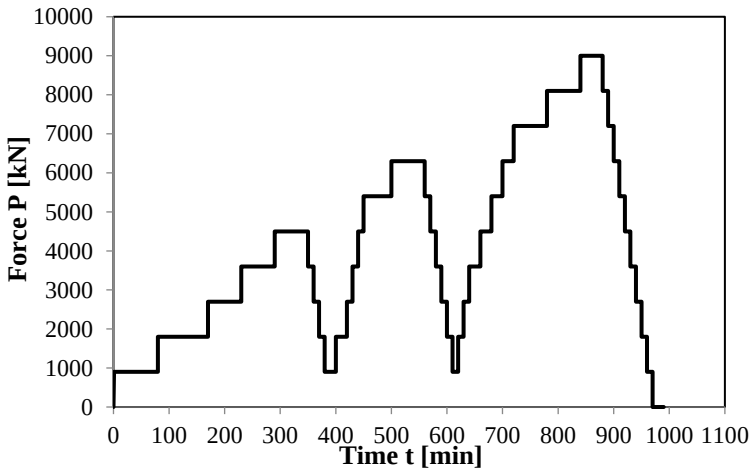

Figure 6. Diagram of the test loading force and time

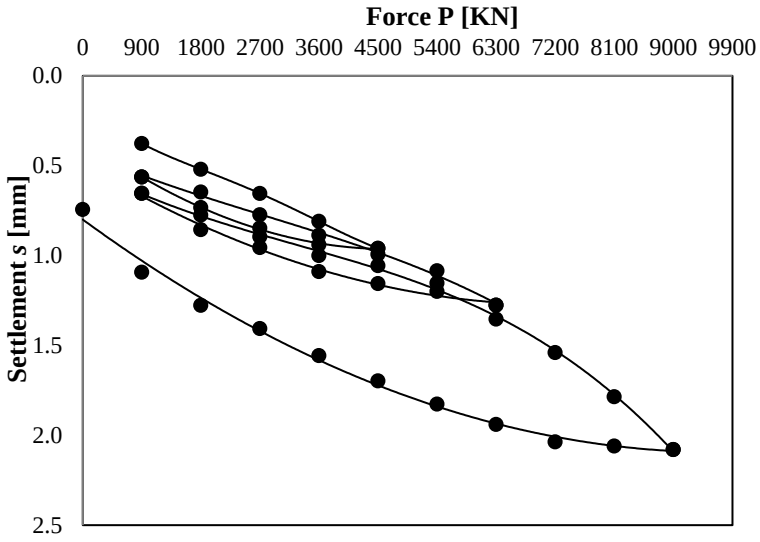

Figure 7. Load-settlements curve of test pile

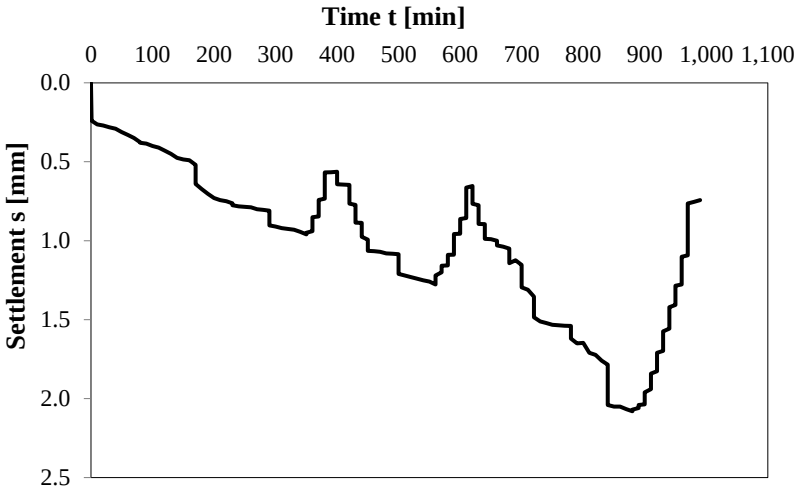

Figure 8. Time-settlement relationship

Table 1. Display of maximum applied force and settlement per load cycle

Loading cycle	Force [kN]	Settlement [mm]
I	4500	0.96
II	6300	1.27
III	9000	2.08

`

It is evident that the design loads cause very low settlements, which only confirms the axial capacity of the pile, which is higher than estimated in the design documentation. This case is probably due to the underestimated material characteristics of the rocky, i.e. semi-rocky material and the fact the pile foundation type is end bearing piles. According to the standards and positive practice in the country, the allowable settlements for such a structure, with a statically indeterminate system, must not be greater than 50.0 mm or as a differential less than 5.0 mm. In this case neither one of the criterion is reached, which implies that the piles are loaded with a force significantly lower than their ultimate bearing capacity.

6. TEST RESULTS

The main objective of the numerical modelling is based on a pre-calibrated model for loads up to 9000 kN, in order to estimate the axial bearing capacity of the pile, having in mind the impossibility of loading the pile with forces close to the ultimate capacity.

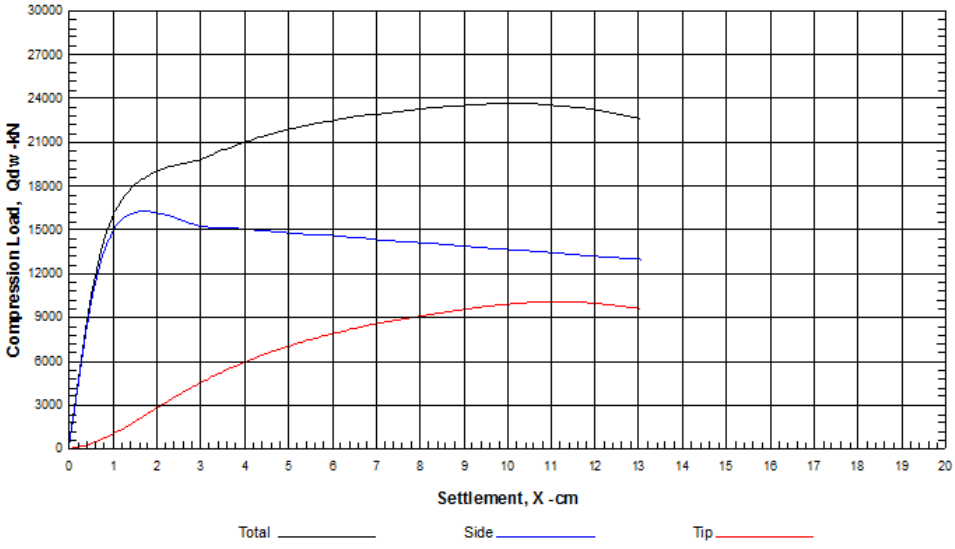

Figure 9. Load-settlement relationship obtained in AllPIle 6.5 software (red: pile base resistance, blue: pile shaft resistance, black: total pile resistance

In the first step, the geotechnical model is calibrated in the AllPile 6.5 software, i.e. reverse analysis for obtaining the physical-mechanical and load-deformation parameters, that will give a maximum settlement of the pile of 2.08 mm. It was confirmed that the parameters were in the limits of those defined in the design documentation and they are: γ=25 kN/m^3, φ=32°, c=200 kPa, E=3000 MPa, k=100000 kN/m^3, υ=0.3. Figure 9 shows the dependence between the settlements and the axial load on the pile, divided into base bearing capacity and bearing capacity along the piles shaft. The total ultimate force is estimated at 23625.84 kN.

7. CONCLUSION

According to the methodology of determining the axial pile bearing capacity in soft graphitic schists, through the procedure of static pile load testing, the ultimate axial load capacity is determined. From the 16-hour testing period of the pile and from the result analysis, it can be concluded that the design loads cause relatively small settlements, lower than the estimated ones within the design and the allowable ones in accordance with the positive practice of testing for such structures, as a statically indeterminate system (SIS). The piles are loaded with a force lower than their bearing capacity, which is also an imperative in the structural design. In order to estimate the reserve and the ultimate bearing capacity, numerical modelling is done by calibrating the parameters of the substrate with the settlements obtained during testing, where an ultimate force of 23.625,84 kN is obtained. For more precise results that will refer to the entire pile foundation, it is recommended for a 3D numerical analysis to be done, taking into account the interaction of the upper (above ground) structure and pile foundation with the surrounding environment.

REFERENCES

[1] Faculty of Civil Engineering in Skopje (2016), Field and numerical testing in determining the load bearing capacity of foundation structures in spatial geotechnical conditions, Science project report.

[2] Susinov, B., Josifovski, J. (2016), Field test report: pile load testing of a Ø1200mm pile from viaduct pile foundations at km 9+105 of A2 state highway (Kichevo – Trebenishta – Ohrid, section Podvis – Preseka, pillar P2, pile no. 16.) Skopje.

[3] Gjorgjevski, S., Jovanovski, M. (2017), Final opinion on the load bearing capacity of piles with analytical calculations on defining the load bearing capacity based on the pile load testing established, Skopje.

Gjorgji Gjorgjiev
PhD, Associate Professor
University 'Ss. Cyril and Methodius'
Faculty of Civil Engineering – Skopje
N. Macedonia
gorgi.gorgiev@gf.ukim.edu.mk

Vancho Gjorgjiev
PhD, Full Professor
University 'Ss. Cyril and Methodius'
Faculty of Civil Engineering – Skopje
N. Macedonia
gorgiev@gf.ukim.edu.mk

Natasha Malijanska Andreevska
MSc, Teaching Assistant
University 'Ss. Cyril and Methodius'
Faculty of Civil Engineering – Skopje
N. Macedonia
malijanska@gf.ukim.edu.mk

BUILDING FOOTPRINT EXTRACTION FROM LIDAR POINT CLOUD DATA

In the past two decades, very intensive development has been done in the area of LiDAR technology, providing high-quality spatial data for large areas in a short time. The raw LiDAR data consists of an enormous number of points, made by reflection of the laser beam from various objects such as earth's surface, buildings, vegetation, powerlines, bridges, etc. In order to extract the geometrical characteristics of the objects many different approaches and methods have been developed. Many of these approaches have been focused on automatic feature extraction. The subject of this paper is to investigate the possibilities for automatic building footprint extraction from LiDAR data provided by the Agency for Real Estate Cadastre, available for the territory of the Republic of North Macedonia.

Keywords: LiDAR, point cloud, automatic building extraction, building footprint

1. INTRODUCTION

The need for three-dimensional spatial modeling of the terrain and objects, with details and quality that significantly exceeds traditional 2D approaches, constantly gains attention as a research topic. This need has been initiated by spatial data users and supported by the development and easier accessibility of LiDAR technology for spatial data acquisition. In this context, the 3D models of urban areas stand out, which represent a powerful foundation for various spatial analyzes and simulations in the field of cadastral systems, telecommunications, urban planning, environmental protection, tourism, navigation systems, etc. The models basically consist of a 3D geometric representation of objects of interest, such as buildings, roads, trees, etc. very often combined with high-resolution aerial or satellite images, forming a realistic model, visually and geometrically, accompanied by attribute data that complements the image of the objects being presented. Considering the potential of available data acquisition technologies, researchers in the field of geomatics are focusing on creating powerful algorithms for extraction and 3D reconstruction of objects, so the models would be as close as possible to the

real objects, which consequently, will provide more accurate spatial analysis and greater power in their application. At the moment LiDAR (Light Detection and Ranging) could be pointed out as a primary technology for spatial data acquisition for 3D modeling, as an extremely fast and precise technology that provides a large amount of data in a short time. In the last decade with the development of powerful algorithms for image processing, photogrammetry took a significant part in this process. Primary objects for creating 3D models of urban areas are buildings, which in practice could have a large variety of shapes, sizes and details.

Depending on the existing data quality, such as point resolution, the 3D model can be produced with different levels of detail. The spatial data acquisition methods when the sensor is placed on an aircraft have an excellent potential for geometrical modeling of the roofs of buildings and limited potential for modeling the walls and other elements of the building that are not visually accessible from a height. In these cases, it is a kind of challenge to create a model for the areas that are not observed with a large number of points. Since the building structure is complex, their complete automatic reconstruction is not yet feasible with a high level of quality. Therefore, manual and semi-automated approaches are still widely used, although it can be said that the automatic detection of buildings, with the algorithms that are available and implemented in software, every day, achieves better results. Considering the fast dynamics for the establishing and updating of 3D models, the automatic detection of buildings and the extraction of their geometric properties are of great importance.

2. POINT CLOUD PROCESSING METHODS

The research in the area of point cloud implementation, as a data source for detailed modeling of urban areas, has revealed a point cloud large potential. In recent years, studies on the detection and reconstruction of buildings have made significant advances (Gilany, S.A.N. 2018). The need for faster, more detailed, and reliable building detection and reconstruction has led to intensive development of many algorithms based on different approaches. In general, the process of building modeling can be separated into two major steps, *building detection*, and *building reconstruction*. The first step deals with the segmentation and classification of points from a point cloud, while the second step comprises the reconstruction of the building based on the classified point cloud data.

Segmentation and classification

Segmentation of point cloud is a process where points are placed in groups with some common characteristics, for instance, geometrical or radiometric characteristics, such as ground and non-ground points. A segmented point cloud consists of points belonging to only one of many predefined segments. In the segmentation algorithms point properties such as reflectance intensity (if it is a point cloud obtained by laser scanning), the number of returns or geometric properties could be used. Typically, in laser scanning data, geometrical properties such as surface normal, gradients, and curvature in the neighborhood are used (Sapkota 2008).

The methods used in the segmentation process are several and in general could be divided as follows (Grilli, F., Menna, F., Remondino, F. 2017):

- Edge-based,
- Region growing,
- Model fitting,
- Hybrid method,
- Machine learning method.

The *edge-based* method consists of two consequent steps, the first step detects the edges that outline borders of different regions/segments and the second step groups the points within detected borders. Edges are detected by the change of a local variation beyond the provided threshold.

The *region growing* method starts from a single point and grows around neighboring points that fit well in a surface with similar characteristics as surface orientation, curvature, etc. The points that are considered as part of the same object, with similar characteristics, are placed in one segment.

The *model fitting* method tries to fit primitive shapes in point cloud data and the points that conform to the mathematical representation of the primitive shape are treated as one segment.

The *hybrid method* takes more than one of the previous methods in consideration during the process of point segmentation.

The *machine learning* method of point cloud segmentation is frequently used. This method takes into consideration successfully segmented point cloud data, learns from the

provided examples, and then gained "knowledge" is implemented on other non-segmented point cloud data. This method is robust and flexible.

The second part of the first step deals with point cloud classification. The classification takes further the segmented point cloud by providing details about points and dividing them into classes such as buildings, high and low vegetation, bridges, powerlines, etc.

Building reconstruction

The second major step after building detection is building reconstruction. Depending on the needs, the reconstruction of the buildings could be done as 2D reconstruction of the building footprint or 3D modelling. Since the major focus in this paper is placed on 2D reconstruction, a short description of the process will be given.

There are a large number of algorithms for the creation of polygons that represent the footprint of the laser scanned building. The paper will briefly discuss two possible approaches to achieve this goal.

The first approach is based on the assumption that the buildings consist of straight lines and the building corners are square angles. Based on this assumption, the polygon is created by fitting many rectangular polygons that are iteratively changed, further reduced or increased in order to establish a complex polygon representing the size of the building from those small rectangular polygons.

The second approach for creating a polygon of the building footprints envisages inserting straight lines that are formed with the support of the points representing the edges of a building. By further processing, the lines are converted into polygons based on their intersections and connections.

The first method gives good results when buildings have square angles and straight sides, while the second method gives good results when the buildings have flat, straight sides, but not always square corners.

3. METHODOLOGY

The primary goal of this research is to investigate the possibilities and quality of the automatic building footprint extraction from LiDAR point cloud data available from the Agency for Real Estate Cadastre in Republic of North Macedonia.

The official data source is the database of the Agency for Real Estate Cadastre (AREC) from the LiDAR scanning activities performed in 2019. It is an airborne laser scanning with a flight altitude of approximately 1200m above the ground. Although the density of points varies, we can say that it is approximately 30 points per square meter. According to the data obtained from the quality control reports for the dataset, controlled through the height difference between the recorded points with classic surveying technics and the points from the LiDAR scanning, a mean square error of 0.025m was achieved, while the positional accuracy according to the control is within 0.06m. During quality control, it was determined that the height difference between two overlapping scanning lines is less than 0.05m.

The data processing consists of several consecutive steps tailored to achieve the highest possible quality. The process begins with the first step, which focuses on removing, i.e., classifying outliers (noise). The second step in the sequence is the segmentation of the points into ground and non-ground points. The third step uses the non-ground points and further classifies the points that represent buildings. The fourth phase refers to the extraction of the building's footprint based on the points belonging to the class "buildings", to finally perform the regularization of the created polygons, i.e., to make a kind of generalization that follows a certain tendency, for example, the expected shape of the buildings, right angles, straight sides, etc. The process is shown schematically in the following graph:

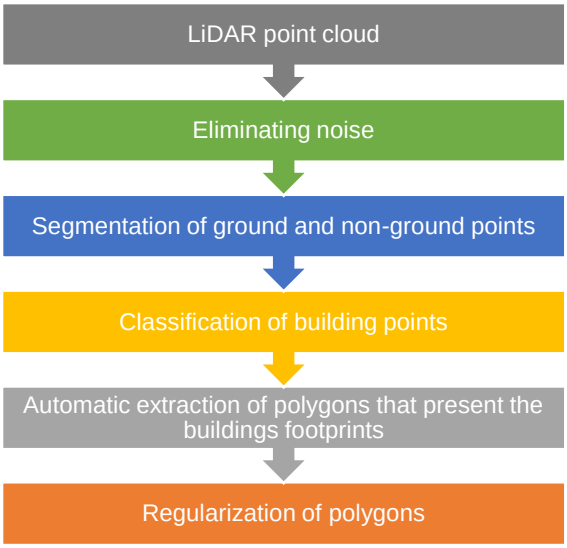

Figure 1. Methodology for automatic extraction of buildings footprints

In order to conduct a comparison of the results obtained by processing the LIDAR data with another reliable and accurate dataset, data from the registration of buildings from the cadastral system is used as reference data. This data is obtained by photogrammetric and classic surveying methods followed by many controls. The comparison is based on the assumption that the buildings analyzed in the research haven't been changed between the moment of registration in the cadastral system and the moment of LiDAR scanning.

To evaluate the quality of the automatic footprint extraction approach, a two-stage process was established. The quality control results of geometric shapes representing building footprints will be expressed in numerical values, but also narratively because the presentation of the matching between detected building footprints and registered building footprints is difficult and it can be misleading if it is only presented by numerical indicators.

The first approach to assess the quality of the detection is made by overlapping the polygons that present the detected building footprints and the polygons that present the registered buildings in the cadastral system. These two objects should be approximately the same in shape and size, but with differences arising from the different modelling approaches. The closer those two shapes are, the higher quality of automatic detection is obtained. Of course, in this research, the data obtained from the cadastral system is given priority in terms of quality.

To show the quality of the results in the first approach, two numerical indicators were used:

a) percentage of the area of the detected building footprint within the registered building footprint,
b) percentage of the area of the registered building footprint within the detected building footprint.

Considering the fact that there are newly erected buildings that have modifications that are not registered in the cadastral system, but those same buildings are detected by processing LiDAR scan, the impression of a large discrepancy between the detected and registered building footprints will be created. For those reasons, such buildings will be excluded from further data analysis. It should also be noted that in the process of automatic footprint detection, objects that are not subject to registration in the cadastral system, such as bus stops, traffic lights, small sheds, etc., will be detected by processing LiDAR scans. These objects will also be excluded from the comparative analysis.

The second approach for the quality evaluation of the building footprint detection is carried out through a visual inspection considering the matching of the two figures. Since it is based on expert opinion, there is always a possibility of subjective conclusions, but if it is done impartially and conscientiously it can be an excellent indicator of the detection quality.

3. RESEARCH RESULTS

As an area for the case study, an urban area with the presence of public, business, and residential buildings was chosen. These buildings are characterized by a large footprint and straight sides usually placed at an angle of 90°. In some parts of the area, close to the buildings, there is a significant presence of high vegetation. The research area covers 37ha, the highest building has a height of 60m, and the largest area under the building is 23200 m2. Based on the automatic building footprint extraction, a total of 105 polygons were created (Figure 2).
As a basic principle for building footprint extraction and comparison, need to be pointed out that extracted building footprints can differ from the building footprints registered at the cadastral system. This is because buildings that are sharing a wall are so close one to another that the detected polygon represents these two or more neighbouring buildings as a single building presented with a single polygon, while on the other hand, the cadastral system could register two or more buildings. This is because the cadastral system makes distinctions and sees more than one building from purely administrative reasons, and not because the geometric characteristics are showing more than one building.

Figure 2. Extracted buildings footprints in the research area (red polygons)

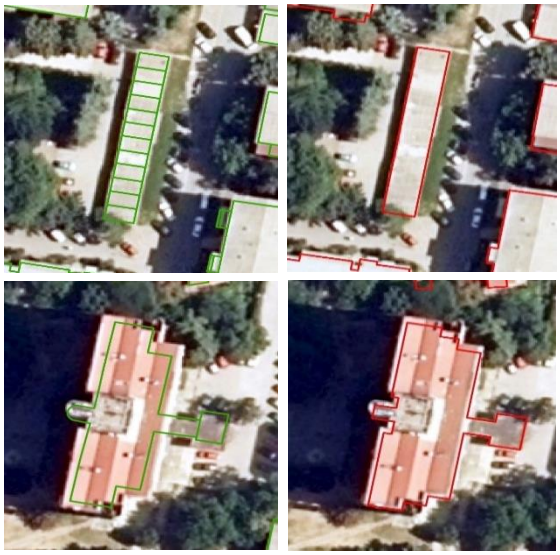

Figure 3. Building footprints registered in the cadastral system (left – green polygons), extracted building footprints based on LiDAR data (right – red polygons)

By comparison of the extracted and registered building footprints, it was calculated the first indicator, and it was found that on average 86% of the area of the polygons of the automatically extracted building footprints is within the polygons of the registered building footprints in the cadastral system. This area overlap varies from the lowest of 69% to the highest overlap of 98%.

Figure 4 shows the result of the comparison of these two datasets, where the horizontal axis shows the percentage of overlap of the extracted polygons within the registered polygons, while the vertical axis shows the number of polygons in the given interval.

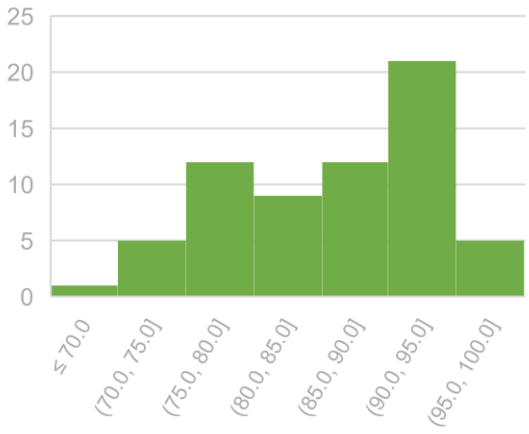

Figure 4. Percentage of overlap of the extracted polygons within the registered polygons

The second numerical indicator shows that the percentage is higher when it comes to the overlap of registered building footprints within the automatically extracted building footprints. The smallest overlap is 64% while the largest overlap is 100%. This means that the polygons from the automatically detected building footprints in a large percentage, and in some cases even completely, contain the polygons of the cadastral registration. The previous statement can be confirmed by the figure, which shows the percentage of overlap on the horizontal axis, and the number of cases in the given interval on the vertical axis. Figure 5 shows that most of the building polygons have an overlap of more than 95%, while only a small part of the building polygons have an overlap of less than 85%.

These two numerical indicators confirm a situation that can also be seen from the visual inspection, which shows that the polygons presenting the automatically extracted building footprint usually cover a larger area than the polygon presenting the registered building footprint. This conclusion is logical, maybe even expected, considering the LiDAR technology and the position of the sensor in relation to the buildings. The canopies, cantilever parts of the buildings, awnings, balconies, etc. significantly contribute these parts of buildings to be shown in an expanded form in comparison to the officially registered building footprint in the cadastral system, where we only have a presentation of the contact between the building and the ground, but not the extensions that are located on a certain height above the ground.

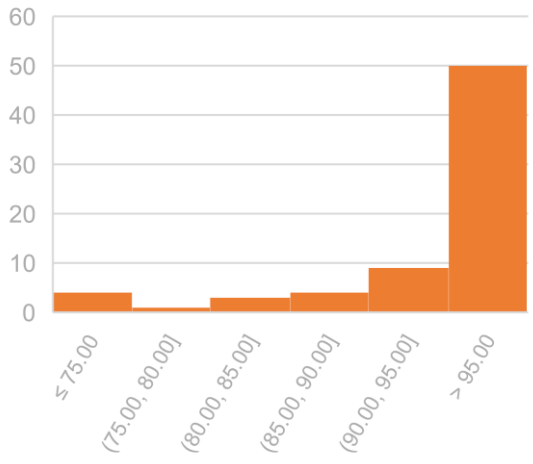

Figure 5. Percentage of overlap of the registered polygons within the extracted polygons

To present the automatic footprint extraction and interpretation of the buildings in more detail and to get an impression of the possibilities and weaknesses of this type of extraction, the results, and cases, of the extraction, will be

presented. The classification of these buildings into three characteristic cases is based on their degree of overlap.

Case 1

The buildings presented in case 1 have a high percentage of overlap between the extracted and the registered polygons in the cadastral system. This type of building is characterized by a simple, rectangular shape, a height of approximately 30m, and does not have large canopies and/or consoles (Figures 6 and 7).

Figure 6. Building footprints registered in the cadastral system (green polygon), extracted building footprints based on LiDAR data (red polygon)

Figure 7. Photograph of the buildings shown in Figure 6

The percentage of overlap of the buildings with characteristics as in case 1, according to the first numerical indicator, more precisely the overlap of the extracted building footprint polygon within the registered building footprint polygon, is on average 94%. The second numerical indicator for this type of building shows an average of 99.5% overlap. The sides of the polygon produced by automatic extraction are parallel to the sides of the registered polygon, the number of vertices is approximately the same, and the polygons have an almost identical shape. The deviations of the vertices range between 20cm and 90cm.

Case 2

The buildings presented in case 2 have a complex shape, many vertices, a relatively small height, and a large area under the building. In general, these are public buildings, schools, kindergartens, shopping centres, etc.

In terms of numerical indicators, we can say that this type of building also has a high percentage of overlap. The first numerical indicator shows that the percentage of the overlap of the extracted polygon within the registered polygon is on average 94%, while the second numerical indicator shows that the percentage of overlap of the registered building footprint within the extracted building footprint is 91.5%.

Figure 8. Building footprint registered in the cadastral system (green polygon), extracted building footprint based on LiDAR data (red polygon)

Figure 9. Photograph of the canopy on the building shown in Figure 8

It could be noted that the shape of the buildings is almost the same and many details have been preserved. For this particular building it can be pointed out that there is an existing canopy and it creates a false impression that the footprint of the building is larger. This location in Figures 8 and 9 is indicated by a yellow circle. It is interesting to note that the openings in the

buildings (patios) in both cases of the building presented in Figures 8 are shown without major deviations regarding the registered polygon in the cadastral system.

Figures 10, 11 and 12 show another building classified as case 2.

Figure 10. Building footprint registered in the cadastral system (green polygon), extracted building footprint based on LiDAR data (red polygon) – Skopje City Mall

Figure 11. Photograph of the building shown in Figure 10 - Skopje City Mall

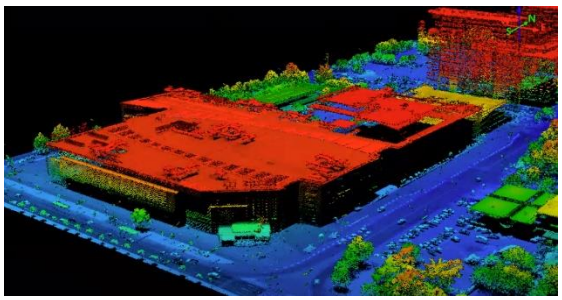

Figure 12. LiDAR point cloud of the building shown in Figure 10 - Skopje City Mall

Case 3

The buildings in case 3 have a greater difference between the polygon produced by the automatic extraction of building footprints in comparison to the polygons registered in the cadastral system. This type of building is shown in Figure 13. If we take a closer look, we can say that the larger deviations occur on the northern side of the building, which essentially represents an open terrace with a height above the ground of approximately one meter. On the other hand, if we look at the point cloud, it can be concluded that the points that present this part of the building (the terrace) are segmented as non-ground points but are not classified as building points. The reason for this situation is that, during the extraction of building footprints, a condition has been set that the points where there is a local variation in height greater than 2 meters should be classified as buildings. Since the open terrace is less than two meters high, the points are not classified as building points. The situation is the same with the points on the eastern side. Figure 14 shows the point cloud related to the specific building, where the points from the terrace are segmented as non-ground points, but not classified as building points.

Figure 13. Building footprint registered in the cadastral system (green polygon), extracted building footprint based on LiDAR data (red polygon)

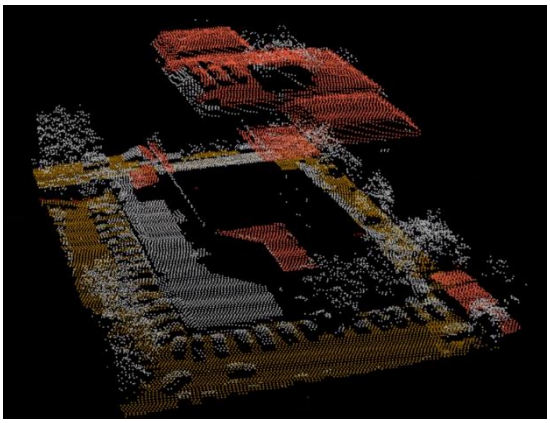

Figure 14. Classified LiDAR point cloud of the building shown in Figure 13 (red points - buildings, gray points – non-ground, brown points - ground)

Figure 15. Photograph of the building shown in Figure 13 – north side

Figure 16. Photograph of the building shown in Figure 13 – south side

The extracted building footprint given in Figure 17 has more deviations in relation to the cadastral registration. This is a characteristic situation in which the building is surrounded by urban equipment, canopies, and umbrellas which according to the law on cadastre are not subject to registration. The points obtained by the LiDAR scanning are classified as building points because those locations have urban equipment with geometric characteristics of buildings.

Figure 17. Building footprints registered in the cadastral system (green polygon), extracted building footprint based on LiDAR data (red polygon)

4. CONCLUSIONS

The first category of conclusions refers to the capability of automatic building footprint extraction based on airborne LiDAR point cloud. The analyses of the results of the automatic building footprint extraction have provided the following conclusions:

a) Building footprint extraction has higher quality in the case of large and tall buildings,
b) The presence of canopy covers creates a false impression that the building footprint is larger than it is,
c) Series of buildings connected by common sidewalls, forming a continuous group are extracted as a single building footprint,
d) Buildings surrounded by urban equipment, umbrellas, canopies, verandas, carports, etc. are creating a false impression of a larger building footprint.

The second category of conclusions focuses on the application of automatic building footprint extraction obtained by processing airborne LiDAR point cloud data. The sublimated conclusions indicated that the building footprints can be used in the following situations:

a) Detection of newly built and unregistered buildings,
b) Detection of extensions/upgrades of existing buildings,
c) Detection of removed buildings and structures.

The third category of conclusions is essentially a part of the second category, but considering its importance, it is pointed out as a separate category. It is about establishing 3D building models as an essential component in the construction of 3D city models. The production of these models is greatly facilitated and shortened on the one hand, and the quality and details are significantly improved on the other hand, if point cloud data is used. It should be noted that further increases in the quality of these models will be achieved by combining the point cloud data and cadastral registration data.

REFERENCES

[1] Arefi, H. (2009), From LIDAR Point Clouds to 3D Building Models, PhD thesis, Universität der Bundeswehr München Fakultät für Bauingenieur- und Vermessungswesen.

[2] Gilani, S. A. N. (2018), Building Detection and Reconstruction using Airborne Imagery and LiDAR Data, PhD thesis, Faculty of Information Technology, Monash University, Australia.

[3] Grilli, F., Menna, F., Remondino, F. (2017), A review of point cloud segmentation and classification algorithms, The International Archives of the Photogrammetry, Remote Sensing and Spatial Information Sciences, Volume XLII-2/W3, 2017.

[4] Kim, A., Plsen R. C., Kruse, F. A. (2013), Methods for LiDAR point cloud classification using local neighborhood statistics, Laser Radar Technology and Applications XVIII, Proceedings of SPIE - The International Society for Optical Engineering, May 2013.

[5] Sapkota P. P. (2008), Segmentation of colored point cloud data, Master thesis, International institute for Geo-Information science and earth observation, Enschede, The Netherlands.

[6] Uygren, P., Jasinski, M. (2016), A Comparative Study of Segmentation and Classification Methods for 3D Point Clouds, Master thesis, Department of Computer Science and Engineering, Chalmers University of Technology and University of Gothenburg, Sweden.

moodle IS @ Civil Engineering Faculty

HOW WOULD YOU TAKE YOUR STUDYING?

STAY IN

TAKEOUT

ON THE GO

we do it all via blended learning

www.gf.ukim.edu.mk

Ditar Memedi
MSc
University 'Ss. Cyril and Methodius'
Faculty of Civil Engineering – Skopje
N. Macedonia

Mile Partikov
PhD, Assistant Professor
University 'Ss. Cyril and Methodius'
Faculty of Civil Engineering – Skopje
N. Macedonia
partikov@gf.ukim.edu.mk

Denis Popovski
PhD, Associate Professor
University 'Ss. Cyril and Methodius'
Faculty of Civil Engineering – Skopje
N. Macedonia
popovski@gf.ukim.edu.mk

FAILURE MODES OF I-BEAM WELDED TO SHS COLUMN JOINT DUE TO CONNECTION MODELING

When it comes to bolted connections, the most used cross-sections for columns and beams are without a doubt the I-profile family. There is sufficient research and theoretical knowledge in the literature to determine the stiffness characteristics of moment connections of this category. The moment connection analysis methodology for this family of sections is known as the Method of Components, developed by Zoetemeiier [6], and which is also adopted in EN 1993-1-8 [2]. This method provides a theoretical evaluation of the three of the most important properties of connections, namely: Strength, stiffness and ductility, and is based on a mechanical model.

On the other hand, cases are not rare when square or circular sections, welded with I-beams, are used for columns, instead of open sections. For this configuration, according to the knowledge of the authors, there is no unified analytical formulation (adopted in the form of a code/rulebook) that would describe the three most important properties of the connections. For these reasons, in design practice, it is often the case for welded connections between square columns and I-beams that the connection is modeled as a fully rigid connection.

In this paper, an approximate method for determining the rotational stiffness for this category of welded connections is proposed, using FEM software, Ideas StatiCA 21.1.

The moment at the joint from an external load, generated by this rotational stiffness, is calculated. The effect resulting from the action of this moment including the deformation of the front face of the column is also considered.

The same deformable effects are calculated when the joint is treated as fully rigid. Finally, a comparative analysis at the level of a frame with a semi-rigid connection and a frame with an ideally rigid connection is conducted. The results and effects of these assumptions are interpreted.

Keywords: semi-rigid connections, rotational stiffness, column face bending, column punching shear.

1. INTRODUCTION

The choice of I and H sections for structural steel frame is more dominant in Europe and the USA in comparison with Japan. In these regions, modular planar frames have been applied, frames where stiffness is dominant in its plane, while around weak axis, stiffness is provided with the help of bracing system. In Japan, the situation is different, where space frames are more dominant [7]. This is achieved with the help of rectangular (RHS), square (SHS) and circular hollow sections (CHS). Depending on the dimensions, they tend to have a more equal distribution of the radius of inertia in the two main directions compared to I-sections.

Conventionally known details from this group are welded I or H beams with RHS columns, as in Figure 1.

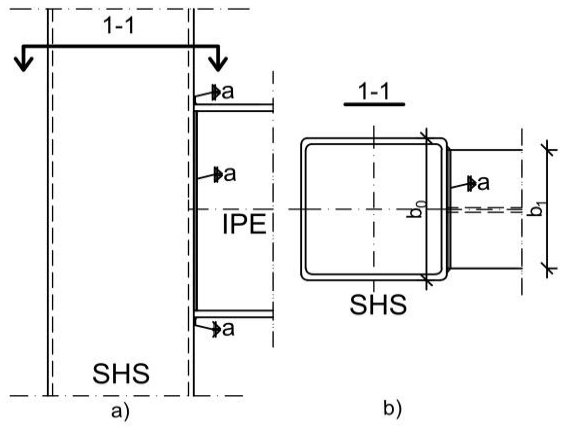

Figure 1. a) Typical welded I-beam to SHS column conncetion, b) base view

In design practice, a welded connection between any steel section is modeled as a fully rigid connection [11, section 2.6] Depending on the geometry of the frame, without taking into account the local stiffness and deformable characteristics of the node itself, a distribution of moments is generated.

Directly proportional to the increase in the cross-section area of the columns (RHS or SHS), the moment in the connection node also increases. If no additional stiffeners are provided in the column side, additional effects are transferred to the column walls. In the following paragraphs, the possible adverse effects in the column face (in the joint region) due to improper treatment of the beam-to-column connection are given.

2. ROTATIONAL STIFFNESS ESTIMATION

A initial step in order to have an idea of the transfer of the negative moment from the beam to the node of the connection, is the determination of its rotational stiffness. The deformability, i.e. the rotation of the connection θ and the negative moment $M_{j,Rd}$ are mutually related by the equation for the rotational stiffness according to the following expression:

$$S_{j,ini} = \frac{M_{j,Rd}}{\theta} \quad (1)$$

In the following figure 2, a numerical model between welded I-beam to SHS column connection is given, where the regions that are activated due to the transfer of moments from the beam to the beam-column connection are shown.

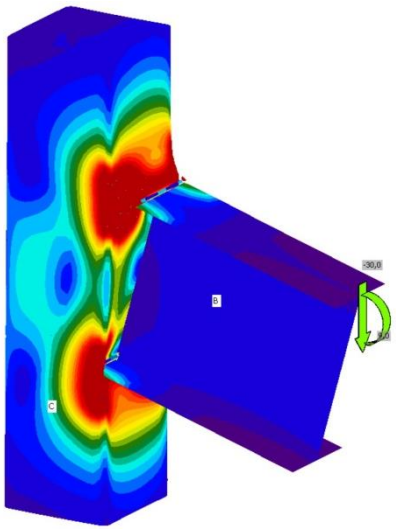

Figure 2. a) Typical physical model between welded I-beam to SHS column connection

The action of the negative moment causes deformations of certain components of the connection itself. In order to mathematically quantify these deformations (the area marked in red, Figure 2), a general approach consists in creating a Model with linear springs. Subsequently, a model is constructed that takes into account these deformed areas of the column, assuming that the beam does not yield in any load combinations.

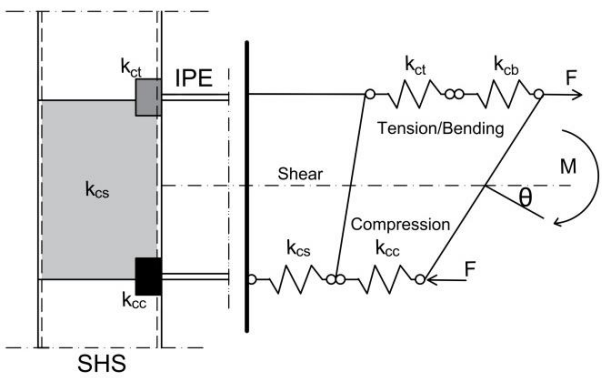

Figure 2. Mathematical model based on linear springs

The active components that make up the mathematical model are:

1. k_{ct} –Column face tension
2. k_{cc} –Column face in compression
3. k_{cs} –Column side wall shear
4. k_{cb} –Column face bending

In the paper of Godoi et al [3], expressions for the determination of the active components for the case of an I-beam welded to a circular column (SHS) are proposed. A model for determining the same active components, only in the case of a rectangular or square column welded to an I-beam, is proposed in the paper [7]. However, there is still no unified explicit solution in the form of a code for determining these active components. For these reasons, in this paper, approximate methods, based on the finite element method, have been used with the help of Idea StatiCA 21.1 software.

The approach to determining the rotational stiffness is as follows:

A welded connection between the beam and the column is modeled using CBFEM (Component-based Finite Element Method) in Idea StatiCa 21.1, [12]. All steel plates are modeled by 2D finite element method assuming ideal elastic-plastic material on the other hand, welds are modeled as nonlinear springs. The transversal load immediately next to the welded joint is calculated, and it is given as an external load in the software. The next step is to apply a bending moment as an external load.

An initial calculation of the connection is performed and the following capacities from the software are read: capacity of welds and the efficiency ratio of the all other components as well as the initial rotational stiffness at that particular step of the analysis.

If it is noted that the efficiency ratio of the all constituent elements is below 90%, it means that the obtained initial rotational stiffness is greater than the real value and the the incremental increase of bending moment $M_{ed,i}$ (*i*-th step) should continue.

The analysis continues in the next step, by gradually increasing the bending moment (keeping the transverse loads constant) and reading the efficiency ratio of the constituent elements and the value of the rotational stiffness.

Such incremental analysis continues until the set moment (incremental moment) does not cause yield of any of the constituent elements to be exceeded and the rotational stiffness of the connection to drop drastically.
The moment value that does not cause yielding of the constituent components, but represents 99% efficiency ratio of the connection, generates the required rotational stiffness.

2.1. MODES OF FAILURE

To describe the modes of failure in connections between welded sections, it is necessary to understand the transfer of forces between the joined elements. According to the studies of Wardier [5], significant types of failures for this type of connections are:

1. Local failure of the beam flange
2. Column face wall plastification
3. Column punching shear
4. Column shear failure

In this paper, only ,,Column face wall plastification" and ,,Column punching shear" are analyzed.

2.1.1. SHS COLUMN FACE WALL PLASTIFICATION

The mechanism that causes this type of failure is the participation of the flanges in the plastification of the column face wall. The largest number of tests simulating the deformation of an I-beam welded to a square hollow section column were made by Makino et al. [9] and Kamba et al. [8]. In these studies, the equations for determining the bearing capacity are derived from analytical models. These equations were modified to fit the numerical data which were assumed to have a deformation of at most $3\%b_0$, were b_0 presents column width.

In this paper, on the column wall bending, only the influence of the flanges is taken into

account. While incorporating the web as well, research and analytical equations are presented in the PhD thesis of Lu [4].

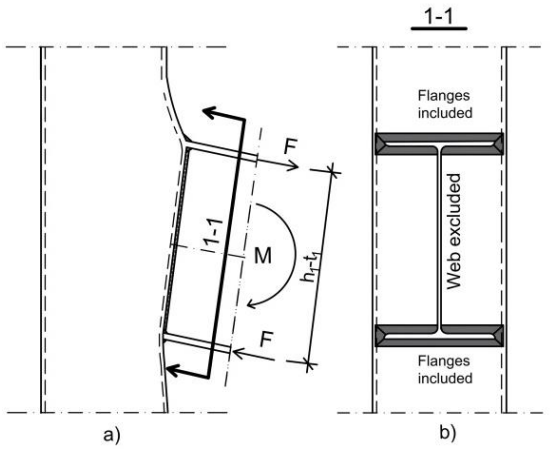

Figure 3. a) Column wall in bending b) Effect of front column face plastification (front view)

Figure 3 a) shows the deformation of the side of the rectangular column under the influence of the negative moment transferred from the I-beam. The magnitude of M is directly proportional to the rotational stiffness of the connection, which needs to be further calculated. The lever arm of internal forces, F, activates the regions in the flanges as shown in Figure 3 b) The bending capacity of the connection under the influence of the moment $M_{Rd_{CWP}}$,, according to [5], is determined by the following equation:

$$M_{Rd_{CWP}} = \frac{f_{0,y} t_0^2 4}{\sqrt{(1-\beta)}} (h_1 - t_1) \qquad (2)$$

,where:

1. $f_{0,y}$ –yield limit for steel
2. t_0 –column wall thickness
3. h_1 –column height
4. t_1 –beam flange width

The coefficient β is a quantity that depends on the ratio between the width of the side of the column in relation to the width of the flange, ie $\beta = b_0/b_1$. This coefficient takes values from 0.45 up to 0.85. When β>0.85, the width of the column flange approaches the lateral sides of the RHS column cross-section, thus the bending capacity increases rapidly, that is, the expression (2) theoretically tends to infinity.

2.1.2. COLUMN PUNCHING SHEAR

The punching shear of RHS(SHS) column from the load transfer of the I-beam, according to the tests of [5] and [10], can be treated as the punching of steel plate in the RHS column. The beam web is located on the softest side of the column face and thus is generally not effective. In the following figure, the active regions (flanges) and their effective compression and tension width b_e are shown.

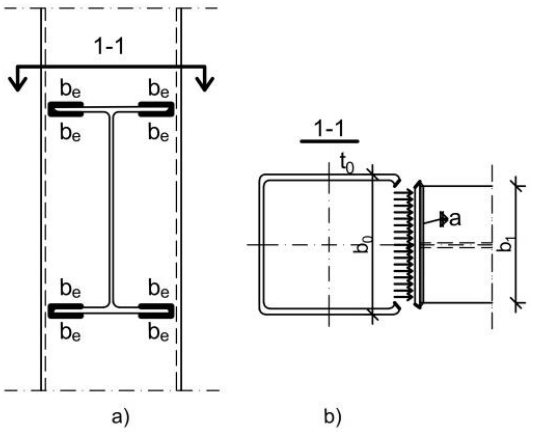

Figure 4. a) Effect of flanges on punching shear of Column b) Column punching shear (top view)

For the same grade of steel for the beam and column, the algebraic expression for determining b_e is given by [3]:

$$b_e = \frac{10}{\left(\frac{b_0}{t_0}\right)} \cdot b_1 \qquad (3)$$

Where b_0, t_0 are the column side width, column wall thickness, respectively.

The force that tends to shear the wall from the column, according to the expression explained in [5] is calculated by:

$$N_{Rd,CPS} = f_0 t_0 (2b_e + 2t_1)/\sqrt{3} \qquad (4)$$

$N_{Rd,CPS}$ acts on pressure and tension, and the figure 4b) illustrates the case when it acts on tension.

3. COMPARATIVE STUDY

3.1.1. DESCRIPTION OF ANALYSED STRUCTURES

In the following, 2 groups of steel frames are analyzed. In the first group, three one-bay, single-story frames are considered where the beam-to-column connection is treated with its corresponding rotational stiffness. A characteristic framework that is the subject of analysis is shown in figure 4.

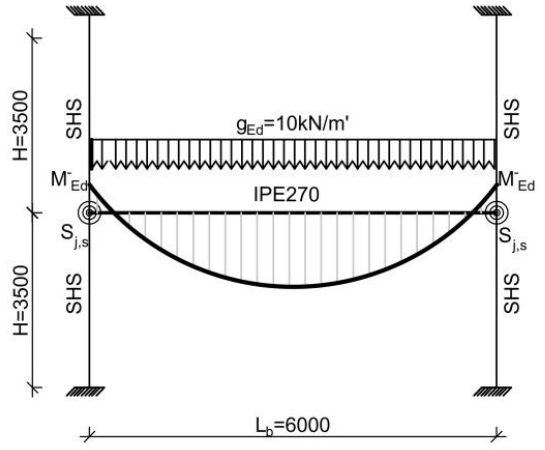

Figure 4. Characteristic one-bay, one story steel frame with semi-rigid connection

The geometric characteristics and the type of sections are given in Table 1, while the steel grade is S235. In the second group, exactly the same frames are analyzed with one difference, the connection between the beam and the column is treated as ideally rigid.

Table 1.Geometric characteristics of the steel frame

SHS column	IPE beam	L_b [mm]	H [mm]
150.150.5	IPE 270	**6000**	**3500**
160.160.5	IPE 270	**6000**	**3500**
180.180.5	IPE 270	**6000**	**3500**

The beam in all connections remains with unchanged dimensions while the geometric characteristics of the column are different. The thickness of the column walls, which in all cases is $t_0 = 5\text{mm}$, meets the condition from the equation,

$$\frac{b_0}{t_0} = c\sqrt{\frac{235}{f_y}} + 3 \qquad (5)$$

recommended by EN 1993-1-8 with the limit equal to 40. In the equation (3), f_y is the steel's yield limit Coefficient c depends on the section class, the cross section and the loadings. For SHS (or RHS), it is conservatively assumed that the width of the "flat" is equal to the external width b or depth h of the RHS minus $3t$. In this situation, $180/5{=}36 < 40$. The difference is in the width of the face walls, varying from $150\ \text{mm}$ to $180\ \text{mm}$.

3.1.2. CALCULATION OF ROTATIONAL STIFFNESS AND THE CORESPONDING HOGGING MOMENT FOR THE FIRST GROUP OF JOINTS

The rotational stiffness and secant stiffness for the three analyzed connections of this group, calculated with Idea StatiCA 21.1, are given in Table 2.

Table 2. Initial rotational stiffness and secant rotational stiffness

SHS column	IPE Beam	$S_{j,ini}$ MNm/rad	$S_{j,s}$ MNm/rad
150.150.5	IPE 270	**12**	**9.1**
160.160.5	IPE 270	**5**	**5**
180.180.5	IPE 270	**2.7**	**2.5**

The rotational stiffness decreases when the width of the column front side is increasing, while retaining the same thickness. According to the data from Table 1, the negative moments from the external load of $p_{Ed} = 10\text{kN/m}'$ were calculated in the joint themselves, for the three connections of the corresponding frames.

Table 3. Hogging bending moments- frame with semi-rigid connections

	150.150.5 IPE 270	160.160.5 IPE 270	180.180.5 IPE 270
$M_{Ed}^{i}[\text{kNm}]$	**13.44**	**12.47**	**10.04**

3.1.3. CALCULATION OF FAILURE MODES

In the following, the failure types for the three connections of the respective frames are calculated.

Table 4. Column face wall plastification ($M_{Rd,CWP}$), column punching shear ($N_{Rd,CPS}$)

	150.150.5 IPE270	160.160.5 IPE270	180.180.5 IPE270
$M_{Rd_{CWP}}[\text{kNm}]$	**18.50**	**14.80**	**11.70**
$N_{Rd,CPS,t}[\text{kN}]$	**18.61**	**17.60**	**15.91**

It is clear from the Table 4 that for the case of a column with smaller cross-sectional dimensions, the load capacity of the column in punching shear or bending is greater compared to the column with dimensions 180.180.5.

3.1.4. CALCULATION NEGATIVE BENDING MOMENT FOR IDEALY RIGID JOINT

As the last step of the analysis is the determination of the negative moments in the joints of the three frames of the same external load, $p_{Ed} = 10\text{kN/m}'$, if the connection is considered ideally rigid.

Table 5. Hogging bending moments- frame with rigid connections

	150.150. 5 IPE 270	160.160. 5 IPE 270	180.180. 5 IPE 270
$M_{Ed}^{i}[kNm]$	**16.65**	**18.49**	**21.10**

It is observed that, with the increase in the dimensions of the column from 150.150.5 to 180.180.5, the negative moment in the connection node gradually increases. In the three considered cases, the negative moment exceeds the permissible loads, according to the type of fracture, shown in Table 5.

CONCLUSIONS

From the results shown in the Table 5, it can be seen that with the increase in the dimensions of the column (width and height), the welded beam tends to act inside from the column face wall. As the outer sides of the flanges are further away from the column outside wall, which also act as "support", the shear or bending capacity is reduced. It should be emphasized that the bearing capacity of the outside column walls, for the same connection configuration and loads, is always greater than the bending or shearing capacity of the column face wall.

According to the results shown in Table 2, it is noted that with the increase in the dimensions of the column, the rotational stiffness, and thus the negative moment in the node of the connection, decreases. These moments, shown in Table 3, are smaller than the bearing moments shown in Table 4.

On the other hand, if the connection is treated as fully rigid, the magnitudes of the negative moments (shown in Table 5) are significantly larger than Column face wall plastification ($M_{Rd,CWP}$) and column punching shear ($N_{Rd,CPS}$) for the corresponding connections (Table 5).

Finally, it can be concluded that, if the coefficient b_0/t_0 is close to the recommended maximum value, from expression (5), and if additional stiffening of the connection itself is not foreseen, then modeling the connection as completely rigid would lead to large hogging moments than the connection capacity itself.

REFERENCES

[1] EN 1993-1-1: Eurocode 3: Design of steel structures – Part 1-1: General rules and rules for buildings, CEN 2005.

[2] EN 1993-1-8: Eurocode 3: Design of steel structures – Part 1-8: Design of joints, CEN 2005.

[3] H. Godoi, M. Miranda, Sarmanho. A, V. Alves: ,,Stiffness assesment of welded I- beam to RHS column connection". Engineering Structures 267 (2022), Departament of Civil Engineering- DECIV, Federal Univesity of Ouro Preto- UFOP, MG, Brazil.

[4] H. Lu: ,,The static strength of I-beam to rectangualr hollow section column connections". Phd Thesis, Delft University Press, Delft, The Netherlands, 1998.

[5] J. Wardier: ,,Hollow sections in structural applications". Delft University of Technology, The Netherlands, 2001.

[6] P. Zoetemeijer: ,,Design method for the tension side of statically loaded, bolted bea-to- column connections", Heron: 20 (1); 1974.

[7] S. Benedetto, M. Latour, G. Rizzano: ,,Stiffness prediction of connections between CHS tubes and externally welded I-beams: FE analyses and analytical study". Materials 2020, 13, 3030.

[8] T. Kamba, M. Tabuchi: ,, Database for tubular column to beam connections in moment resisting frames", IIW doc. XV-893-95, Dep. Of Architecture, Faculty of Engineering, Kobe University, Japan, 1995.

[9] Y. Makino, Kurbobane. Y: ,, Recent research in Kumamoto University in tubular joint design". IIW Doc XV-615-86, XV_E_86-108, p.28, Fac, of Engineering, Kumamoto University, Tokyo, Japan, 1986.

[10] Y. Makino, Y.Kuraobane, K. Orita and Hiraishi: ,, Ultimate capacity of gusset plate-to-tube joint under axial and in-plane loads". Porc. Tubular Structures 4th Internaional Symposium Delft 1991.

[11] COST C1: „Semi-Rigid Behaviour of Civil Engineering Connections", Compoiste steel-concrete joints in braced frames for buildings .Published by the European Commission, European Cooperation in the Field of Scientific and Technical Research, Brussel, 1996.

[12] Waldt et al.: ,,Component-based Finite element Design of Steel Connections". Published by Czech Technical Univeristy in Prague, 2021.

Ditar Memedi
MSc
University ‘Ss. Cyril and Methodius’
Faculty of Civil Engineering – Skopje
N. Macedonia

Denis Popovski
PhD, Associate Professor
University ‘Ss. Cyril and Methodius’
Faculty of Civil Engineering – Skopje
N. Macedonia
popovski@gf.ukim.edu.mk

Mile Partikov
PhD, Assistant Professor
University ‘Ss. Cyril and Methodius’
Faculty of Civil Engineering – Skopje
N. Macedonia
partikov@gf.ukim.edu.mk

COMPARATIVE STUDY ON HOGGING AND SAGGING MOMENT REGION OF STEEL–CONCRETE COMPOSITE FRAME BASED ON CONSTRUCTION STAGES

Many commercial software are unable to provide an overview of displacement, i.e. internal static quantities, when it comes to composite steel-concrete frames. The problem arises precisely because of the variation of the stiffness of composite beam in the region of positive and negative moments along its length. It is well known that the problem can be solved numerically by modeling the composite beam using a finite element mesh, however dividing the beam into finite elements requires knowing in advance where the bending stiffness change for each beam, which basically explains the idea of this paper.

In this study, the equivalent bending stiffness of composite beam as part of a composite frame is analyzed.

Determination of the region of negative moments is calculated depending on the phase of loading, according to the principle proposed by Wong [8].

Depending on the loading phase, geometrical and mechanical property of the beam as well as the stiffness of connection, different lengths of these regions are generated. Determining the exact values of these regions is in principle a long and complicated procedure and that is why, for example, considering Eurocode 4, at each end, 15% of the composite beam length is suggested as one of the negative moment segments, and the reminder of the span is defined as the positive moment segment,
In this study, to investigate the length of these regions depending on the phase of loadings, five composite frames subjected to the same level of loads, but with different levels of rotational stiffness are considered. Moreover, with the help of this method, a comparative analysis was made with the proposals from EN 1994-1-1.

Keywords: equivalent flexural stiffness, semi-rigid connections, rotational stiffness, composite steel-concrete frame beams.

1. INTRODUCTION AND MAIN CONCEPTS

The stiffness of the composite frame beam subjected to vertical loadings varies considerably according to weather the section is subjected to hogging or sagging moments. In the hogging region, the slab is subjected to tension, that's why, it's excluded in the overall bending stiffness of composite beams. While in the zone of positive moments, the concrete section together with the steel section contribute to the significant increase in the bending stiffness due to composite effects.

For such variable stiffness along the length of the beam, simplified models to predict an acceptable constant effective beam stiffness that may be used in analyses are proposed by Leon [2].

$$I_{equ} = 0.4I^{-} + 0.6I^{+} \qquad (1)$$

Where I^{-} and I^{+} are the effective second moment of intertia of the composite beam hogging and sagging region, respectively.

In reality, the problem in determining this equivalent stiffness arises because it is directly dependent on:

- the geometric and mechanical characteristics of the beam and column of the frame
- the amount of tensile reinforcement
- the initial rotational stiffness of the beam-column connection,
- construction phase and the degree of shear connectors
- the intensity and type of loads, as well as from their distribution along the length of the beam.

A combination of all these parameters and their mutual interaction is a complex task for researchers in the field of composite steel-concrete structures. The procedure proposed by Wong, which in principle defines the region of negative moments of a composite beam, covers most of the above inter-related functional parameters.

2. WONG MODEL ONE ESTIMATION OF POSITIVE AND NEGATIVE MOMENT REGIONS

To determine the actual equivalent moment of inertia of the composite beam, the determined equivalent stiffness of beam-column connection, R, should be integrated in the mathematical model of composite frame using the procedure according to Wong [7].

The coefficient of connection (R) algebraically is described with:

$$R = \frac{S_j L_B}{EI_{hog}} \qquad (2)$$

- S_j –secant stifness
- L_B –the span of frame
- EI_{hog} –flexural rigidity of composite beam in hogging reion

For this purpose, the stiffness coefficient R is first determined, and the other parameter (α_{ws}) is read from the interaction diagrams.

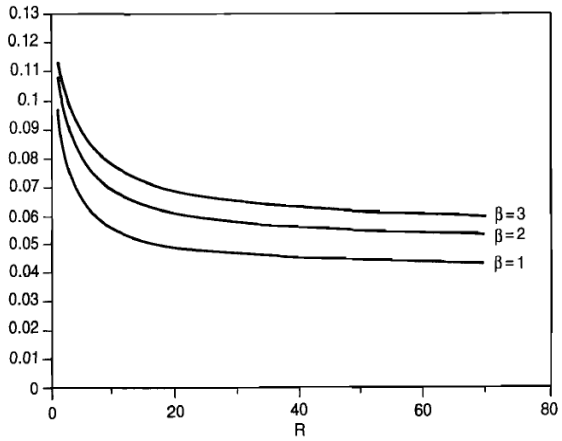

Figure 1. Interaction diagram between R and α_{ws} (Wong,[7])

The diagrams created by Wong are valid if the stiffness of the beam is at most three times the stiffness of the beam over support (bare steel beam).

The curves in this interaction diagram depend on the ratio of the moment of inertia of the beam in the sagging region to the moment of inertia of the beam over the support i.e.:

$$\beta = \frac{I_{sag}}{I_{hog}} \qquad (3)$$

2.1 ANALYTICAL MODEL

The moment of inertia in a midspan, for composite beams, is a variable value, i.e., it depends on the loading phase. Accordingly, the bending stiffness also change from phase to phase. It is usual for the stiffness of the beam to be the highest during the short-term loads

phase and the lowest during the permanent loads + yielding phase. From the diagram (Figure 1), a value for the coefficient α_{ws} is read and the following coefficient is determined:

$$\zeta = \frac{1-\sqrt{1-8(0.125-\alpha_{ws})}}{2} \quad (3)$$

The quantity ζ is known as the coefficient of variation of the stiffness characteristics of the coupled beam. While the value defined by $L\zeta$ describes the region where the beam is in the tension zone. The picture under b) shows a composite beam as an integral part of a coupled frame. In the $L\zeta$ region, the beam is subjected to a negative bending moment. In this area, the steel section and tension reinforcement contribute to the bending stiffness, while the concrete section is neglected in the stiffness contribution.

Combining the region of negative moments with that of positive moments is achieved by determining the equivalent stiffness of the composite beam (Figure 2 under b).

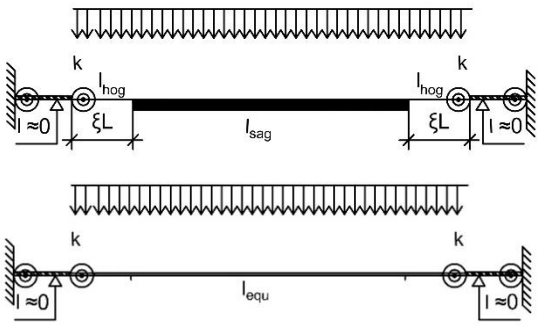

Figure 2. Composite frame beam model -variable stiffness b) composite frame beam model with equivalent stiffness

Equivalent stiffness is calculated as:

$$I_{equ} = \frac{\beta}{(1-\beta)(1-2\zeta)^2+\beta} I_{hog} \quad (4)$$

With expression [4], compared to Leon [5] expression, a more realistic picture of the stiffness of the composite beam in the composition of a coupled frame is obtained. This is due to the fact that in this expression, the stiffness is given as a function of the secant stiffness S_j, ratio of I_{sag} to I_{hog}, type and intensity of loads, α_{ws}, and finally the region where the beam is in the tension zone, ζ.

2.2 ANALYTICAL MODEL BASED ON EC 4 1994-1-1

To determine the effective width of the concrete composite slab, EN 1994-1-1 treats the beam as a static system: continuous beam of several supports.

Namely, due to the effects of semi-rigid connections, a certain negative moment that would appear near the support would reduce the proposed effective widths of the composite slab.

In the analysis of braced frame structures, a range of parameters should be considered to evaluate the correct width of the composite slab, as well as the region of negative moments. It is evident that EN 1994-1-1 does not reflect the real situation and because of this, Eurocode 4 [4] and GB 50017-2017 [6] recommend 15% of the span between two columns to be taken as a region of negative moments while the rest (70%) of the span, for a region of positive moments.

In the next paragraph, an analytical comparison is first made between the approach implemented by Wong [6] and the above recommendation.

3. COMPARATIVE STUDY

To explain the difference between the proposed procedure and the EN recommended value, in this study, two comparisons are made. The first is a fully analytical procedure based on the classification system for semi-rigid connections proposed by EN1993-1-8 [5] and Chen, W.F, 2011 [2].

The second one is based on the analysis of several frames with semi-rigid connections with different value of connection coefficient R.

3.1 THEORETICAL COMPARASION BETWEEN EC 4 1994-1-1 AND WONG'S PROCEDURE

In order to explain the difference, if the same region is calculated according to Wong's procedure, the expression for (3) is considered as a function of the variable α_{ws}.

From Figure 3 it can be observed that the function $\zeta = \zeta(\alpha_{ws})$ is monotonically decreasing and the minimum of the function $\zeta = \zeta(\alpha_{ws})$ is attained for $\alpha_{ws} = 0.125$. This

means that for $\zeta = 0$, the composite beam is treated ideally as a simple supported beam.

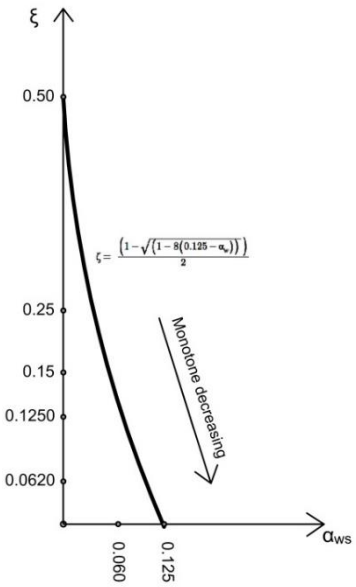

Figure 3. Monotone decreasing function of parameter ζ=ζ(α_{ws})

The coefficient R, in most cases takes values in the interval from 0.5 to 8 [2].

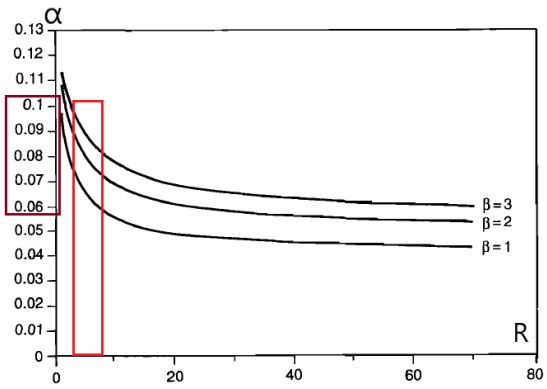

Figure 4. Predicted values for the coefficient α_{ws} based on Chen, [4]

That is, the values for the coefficient α_{ws} are in the interval from 0.060 to 0. 100. Using the function $\zeta = \zeta(\alpha_{ws})$, the values for $\alpha_{ws} \in [0.060, 0.100]$ are mapped to the interval presented in Figure 5.

It is worth noting that no matter how small the degree of shear connection value is, the quotient between I_{sag} and I_{hog} ,that is, the coefficient β, is a value greater than 1. For these reasons, the interval is set aside for values greater than 0.06.

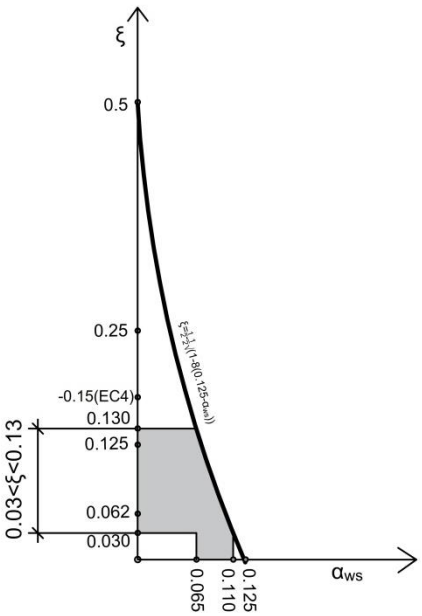

Figure 5. Segment of negative moments as a functional dependence of the parameter α_{ws}

This means that the maximum length of the region of negative moments according to this approach is 13% of the span between two columns.

A value of 0.15, according to this approach, would be obtained if $\alpha_{ws} = 0.060$. From the diagram, such a value for α_{ws} if $\beta \approx 1$ i.e. $I_{sag} \approx I_{hog}$, which means that it is a pure steel beam.

3.2 NUMERICAL COMPARASION BETWEEN THE TWO CONCEPTS

Five one-bay two story braced frames under 12.15 kN/m' gravitational loading conditions are analyzed with the help of Autodesk Robot Structural Analysis 2017. Frames are fixed in the base while the beam-column connection is treated as semi-rigid bare steel connection and its initial rotational stiffness is computed with the help of IDEA StatiCa 21.1 by CBFEM method. The secant stiffness is calculated according to EN proposals, That is, by reducing the corresponding initial stiffness by 50%. The necessary geometric characteristics for solving the frames are shown in a table.

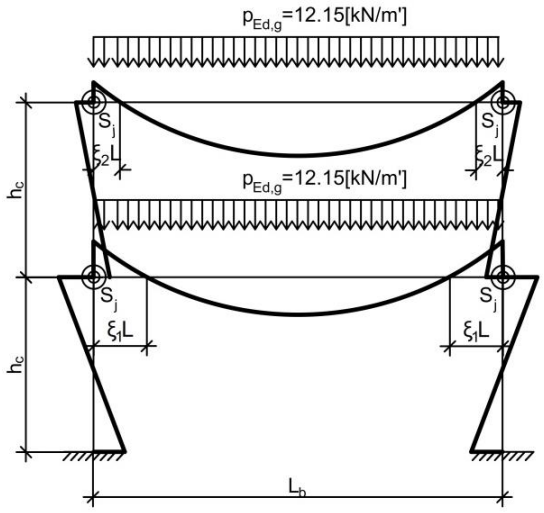

Figure 6. Calculation model

For all frames, an effective concrete section height of 6cm (effective section) above the rib of the profile is taken into account in the analysis.

In **Phase I**, the frame is treated as a bare steel frame with semi-rigid connections. From given loads (12 kN/m') and geometric characteristics of the frames (Table 1), the length of the region of negative moments (ζ') for the five frames was calculated using Robot Structural Analysis.

From the conducted analysis, it is concluded that the lowest value of the region of negative moments was obtained, as accepted, for **Frame 1** in story 2 and its value is 3% L_B. For smaller spans, the rotational stiffness of the beam-column connection has relatively low values (in this case R=0.70) and it induces small values of the region of negative moments. It can be concluded that the composite frame beam can be treated with high accuracy as a simply supported beam with zero negative moment segment.

On the other hand, for the same frame, for story 1 the region of negative moments it is 6.5%. This is due to the fact that in story 1 we have the continuity of the columns that contribute to increasing the rotational stiffness of the column-to-column connection.

For **Frame 2**, slightly higher values are obtained, ie 8.8% L_B and 6.4% L_B for story 1 and story 2, respectively.

Higher length of the region of negative moments is obtained by increasing the span of the frame and specifically for **Frame 3** with L_B =14000 mm story 1 that value is 10%.

Table 1. Calculated parameters

	Frame 1 IPE330-HEA220		Frame 2 IPE500-HEA340		Frame 3 HEA650-HEA450		Frame 4 HEA800-HEA450		Frame 5 HEA900-HEA500	
	Story 1	Story 2	Story 1	Story 2	Story 1	Story 2	Story 1	Story 2	Story 1	Story 2
L_b [mm]	4500	4500	8000	8000	14000	14000	19000	19000	23000	2300
h_c [mm]	2800	2800					5000	5000	5000	5000
S_{ini} [MNm/rad]	16.20	7.70	75	46.60	196	104.4	457	233.80	854	428
S_j [MNm/rad]	8.10	3.85	37.50	23.30	98	52.2	228.50	116.90	427.0	214.0
ζ'	6.8%	3.5%	10.6%	7.5%	11.4%	7.8%	15.2%	13.9	14.2	13.1
I_I	11766	11766	48198	48198	175200	175200	303400	303400	422075	422075
$I_{id,II}$	22266	22700	79230	81489	260913	273496	449297	453578	633591	633591
R	1.47	0.70	2.96	1.841	3.72	1.98	6.81	3.50	11.56	5.79
β	1.90	1.9	1.65	1.70	1.48	1.56	1.42	1.45	1.5	1.5
α_{ws}	0.097	1.10	0.085	0.095	0.08	0.088	0.068	0.078	0.065	0.070
ζ	6%	3.5%	8.8%	6.4%	10%	8%	13.20%	10.5%	13.9	12.58

The obtained values are shown in the table 1.

The next step is the analysis of of the frames is **Phase: Permanent loads** in addition of concreter creep effects.

The resulting moments of inertia, $I_{id,II}$ for the corresponding frames of this loading phase are also shown in the Table 1.

Such a value is expected due to the rather large value of the initial rotational stiffness, which is 92 MNm/rad and its corresponding connection coefficient R=3.72.

However, also for frame 3 the length of the negative moment region is much lower than the recommended 15% by EN 1994-1-1 [4].

Frame 4 was analyzed. The span is 19,000 mm, while the secant rotational stiffness, according to the calculation using IDEA StatiCA 21.1, is 228.50 MNn/rad, 11.60MNn/rad for floor 1 and floor 2, respectively. The connection coefficient, which equals 6.81 and 3.50 for floor 1 and floor 2, respectively, shows that the connection is in the interval of semi-rigid connections, i.e. both values are smaller than the proposed limit, which is 8.

For this example, it is noted that the length of the region of negative moments for floor 2 has a value of 8% L_B while for floor 1 that value is 13% L_B.

Finally, **Frame 5** is analyzed. The column beam connection in this case has the highest value compared to all previous frames. The semi-rigid connection coefficient for this example for floor 1 is R=11.56. Such a value indicates that in this level, the beam-column connection can be treated as a ideally rigid connection, and this is due to the fact that such a value of the coefficient R is beyond the interval of semi-rigid connections proposed by EN 1993-1-8. In the first phase, the length of the region of negative moments, according to the values shown in the table, is 3400 mm (14% L_B) and 2600 mm (10.8% L_B) for story 1 and story 2, respectively.

For story 1, it is evident that the assumption proposed by EN 1994-1-1 of 15% L_B is relatively correct. In the second phase, i.e. in the gravitational loading + concrete creeping effects phase, the length of this region is 13.9% L_B and 12.58% L_B for story 1 and story 2 respectively.

CONCLUSIONS

From the conducted analysis, it can be clearly stated that even for connections that in principle belong to the area of ideally rigid connections, when considering the composite frame beams, due to the high mid-span bending stiffness of the beam, the region of negative moments obtains value lower than 15% L_B.

It should be noted that if the analysis for the determination of these regions is carried out with the secant rotational stiffness of a semi-rigid composite connection, even lower values of these segments should be expected.

On the other hand, completely neglecting these regions, that is, treating the adjacent beams as an ideally pinned connection, has negative consequences in the beam-column connection itself. Namely, the partial negative moment, which in reality exists due to the rotational capacity of connection itself, is in reality transferred from the beam to the column. If this quantity is not taken into account, it is possible to have negative side-effects on the load capacity of the column itself.

REFERENCES

[1] ANSI/AISC 360-10, AISC Committee, Specification for Structural Steel Building; American institute of Steel Construction: Chicago.

[2] Chen, W. F. and Lui, E. M. ,,Stability design of steel frames“ CRC Press, 1991.Eurocode - Basis of structural design.

[3] EN 1993-1-1: Eurocode 3: Design of steel structures – Part 1-1: General rules and rules for buildings, CEN 2005.

[4] EN 1994-1-1: Eurocode 4: Design of composite steel and concrete structures – Part 1: General rules and rules for buildings, European Committee of Normalization.

[5] EN 1993-1-8: Eurocode 3: Design of steel structures – Part 1-8: Design of joints, CEN 2005.

[6] GB 50017-2017: National standard of the People's Rebuplic of China UDC

[7] Y.L. Wong, T. Yu, S.L.Chan. ,,A simplified analytical method for unbraced composite frames with semi-rigid connections“ Jurnal of Constructional Steel Research, 63(2007), 961-969.

[8] Y.L.Wong, S.L.Chan, D.A.Nethercot: ,,A simplified design method for non-sway composite frames with semi-rigid connections“, The Structural Engineer, Jurnal of the Insitution of Structural Engineers, 1996, 74(2):23-8.

PROPAGATION OF FLOOD WAVE CAUSED BY TAILINGS DAMS FAILURE

Ljupcho Petkovski
PhD, Full Professor
University 'Ss. Cyril and Methodius'
Faculty of Civil Engineering – Skopje
N. Macedonia
petkovski@gf.ukim.edu.mk

Stevcho Mitovski
PhD, Associate Professor
University 'Ss. Cyril and Methodius'
Faculty of Civil Engineering – Skopje
N. Macedonia
smitovski@gf.ukim.edu.mk

Frosina Panovska
MSc, Teaching Assistant
University 'Ss. Cyril and Methodius'
Faculty of Civil Engineering – Skopje
N. Macedonia
fpanovska@gf.ukim.edu.mk

Embankment dams' failure is often caused by overtopping during flood wave – caused by insufficient spillway capacity. Failure can also be caused by progressive seepage through the dam's body as a result of increased contact seepage alongside an internal manmade waterway. Other causes for dam failure, include: slope instability of embankment dams, damages in the dam body caused by earthquakes, liquefaction of earth dams under static and seismic action, and flood waves caused by earthquake – induced landslides into the reservoirs from the valley sides [1]. According to ICOLD, the most common reason for embankment dams' failure is overtopping – 30÷35% of all registered cases. During dam failure, as result of the immediate discharge of the impounded water in the reservoir – or impounded flotation tailings at tailings waste lagoon - in the downstream river valley, a catastrophic flood wave makes its hazardous way towards destruction. Normally, the time needed for the flood wave warning system to activate, is much shorter than the time needed for the formation of the flood wave caused by rainfall – runoff. Thereafter, depending on the location of the dam, a potential dam failure – especially in case of tailings dam failure – could result in catastrophic losses of human lives, destruction of agricultural land and long-term degradation of the environment. In this manner, as follows, results of 2D analysis for flood propagation at a cascade system of tailings dams Sasa 3-2 and Sasa 4 are analyzed. Both cascade dams are located in the northeast part of RN Macedonia, on river Saska. The analysis is conducted with the use of the software program HEC RAS.

Keywords: flood wave, dams, tailings, failure, 2D analysis, HEC RAS

1. INTRODUCTION

Tailings storage facilities (TSF) are a special type of structures comprised of a tailings dam and waste lagoon, built to store mud and waste tailings from mining technological process. During the service period of tailings storage facilities (TSF), flotation tailings with hydro transport (usually gravitational pulp line) is transported to the tailings dam crest. There, with hydro-cycloning, tailings separate into two fractions. With the coarser, or dry fraction

(cycloned sand), the dam body is created, and the finer fraction (cyclone mud) is deposited in the waste lagoon.

Currently, thousands of tailings dams worldwide contain billions of tons of waste material from mineral processing. TSFs should be constructed to achieve a safe, stable post – operational tailings pond [2] [3] and to contain the waste materials indefinitely [4]. Therefore, they are supposed to last forever, however, since 1960 there have been over 80 major TSFs failures reported around the world, with the last one reported on January 31st 2023 in Kearl oil sands mine, Alberta, Canada [5].

On January 25, 2019, tailings dam No. 1 of Vale's external link Córrego do Feijão iron ore mine near Brumadinho, Região Metropolitana de Belo Horizonte, Minas Gerais, Brazil, suddenly failed, releasing almost its complete holdings of 12 million cubic meters of tailings in a big burst. As a result, 267 people have been declared deceased and many others as missing [5].

On Aug. 4, 2014, the tailings dam of Imperial Metals Corp.'s Mount Polley copper and gold mine near Likely, British Columbia, Canada, failed, releasing 7.3 million m^3 of tailings, 10.6 million m^3 of water, and 6.5 million m^3 of interstitial water into the environment. The tailings flowed into adjacent Polley Lake and Quesnel Lake, snapping countless trees in its 50 m wide flow path [5].

2. CASE STUDY

Within the zinc and lead mining complex 'Sasa', located in the northeast part of RN Macedonia some 12km upstream from the city of Makedonska Kamenica, five cascade tailings storage facilities (TSFs) are formed: TSF Sasa 1 at 1035 masl, TSF Sasa 2 at 1015 masl, TSF Sasa 3-1 at 995 masl, TSF Sasa 3-2 at 978 masl and TSF Sasa 4 at 952 masl. The fifth TSF – TSF Sasa 4 – is currently in service period (Figure 1).

All TSFs are located in the riverbed of Saska river (also known as 'Kamenichka river'). The river itself has been permanently diverted by diversion tunnel under the right bank.

TSFs Sasa 1, 2 and 3-1 had been formed over 30 years ago and in the past period, their waste lagoons have mostly consolidated and hardened.

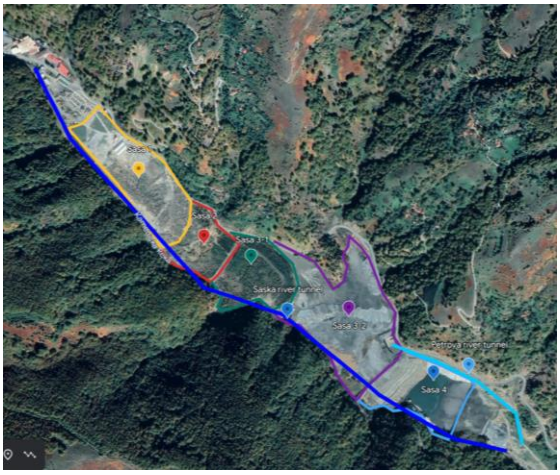

Figure 1. Layout configuration of all five TSFs in the zinc and lead mining complex 'Sasa'. The diversion tunnel for Saska river is under the right bank, whereas the tunnel for Petrova river is under the left bank. Source: Google Earth

TSF Sasa 3-1 is no longer in service since 2003, when an accident occurred with the drainage system. During this accident, a large crater was formed in the waste lagoon Sasa 3-1 (Figure 2), and mudflow propagated downstream in the river valley. The height of the flow was around 10m, and the flood wave reached 12km in length. It is assumed that some 70 000 – 100 000 m^3 of tailings was discharged in the river valley and subsequently in Kalimanci lake [4]. Today, two decades after the accident, downstream of TSF Sasa 3-1, the waste lagoon of Sasa 3-2 is located. It is assumed that the sand dam of Sasa 3-1 keeps the lagoon stable and the risk of mud propagation from Sasa 3-1 is minor [6].

Figure 2. Picture of the visible part of the crater formed in the lagoon of Sasa 3-1

Currently in operation stage is TSF Sasa 4, which is created with construction of a combined tailings dam, with crest elevation of 932.0 masl in October, 2022 (Figures 3 and 4). Designed crest elevation of the tailings dam Sasa 4 is 952.0 masl, with maximal waste lagoon elevation of 950.0 masl.

Figure 3. Downstream tailings dam Sasa 4, waste lagoon of Sasa 4, and upstream tailings dam Sasa 3-2. Picture dates from October, 2022

Figure 4. Downstream slope of tailings dam Sasa 4. Picture dates from October, 2022

Since tailings storage facilities pose major hazard for the downstream river valley, it is crucial to know the potential flood wave propagation area in order to minimize the damaging environmental and social impacts. Dam breach inundation studies are required to evaluate the potential impacts of hazards associated with TSF at all stages of design, whether the facility is proposed, operating or closed [7].

In this paper, the propagation of a potential flood wave caused by dam breach of TSFs Sasa 3-2 and Sasa 4 are analyzed and discussed. It is assumed that the upstream TSFs (Sasa 3-1, Sasa 2 and Sasa 1) no longer pose threat to the downstream valley.

3. DESCRIPTION OF ANALYSES

In the following analyses, a simultaneous cascade dam failure is analyzed for both TSF Sasa 3-2 and Sasa 4, constructed up to their designed crest elevations – TSF Sasa 3-2 crest elevation at 978.0 masl, and TSF Sasa 4 crest elevation at 952.0 masl. Dam breach is presumed up to the crest of their respective initial dams – for Sasa 3-2 the final bottom elevation of the breach is 937.5 masl, and for Sasa 4 – 906 masl.

Storage areas for both Sasa 3-2 and Sasa 4 are defined through volume – elevation curves (Figures 5 and 6).

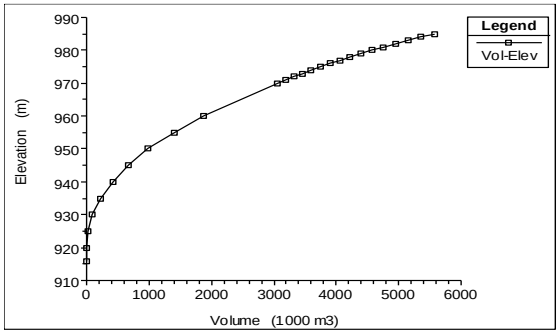

Figure 5. Volume – elevation curve for Sasa 3-2 TSF

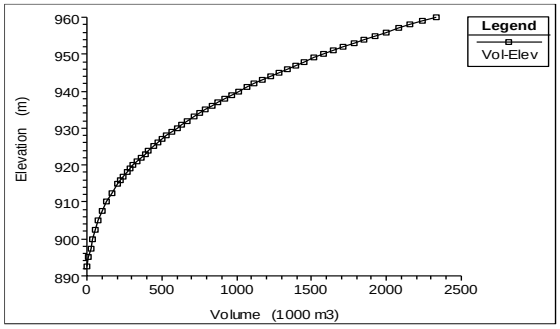

Figure 6. Volume – elevation curve for Sasa 4 TSF

Two scenarios were modelled and discussed.

First scenario assumes waste lagoons at normal operating levels, and dam failure in static conditions, with rainfall – runoff conditions equal to dry state. This scenario is a replica of a situation where an earthquake occurs, or, unfavorable seepage through the tailings dam is the failure cause [6].

The second scenario assumes dam failure caused by overtopping, with flood wave formed with rainfall – runoff from the upstream basin of Petrova and Saska river with probability of occurrence of for return period of T=10 000 years [6].

The analyses were conducted with application of program HEC RAS 6.3.1. Topographic bases were derived from Lidar maps, with pixel accuracy of 10x10m. The model was prepared for 2D analysis, with the use of RAS Mapper. The roughness coefficient is presumed to 0.06 for the whole inundation area, since major part

of it is under natural grassland, woods and pastures.

Like most forensic studies, and all predictive, emergency-management simulations, the following models did not have in situ concentration measurements or rheological data. These parameters can be difficult to measure in controlled laboratory settings. They are practically impossible to measure directly during an event of this scale, which is unpredictable, dangerous, and includes clasts larger than any sampler. Therefore, the fluid is modelled as non – Newtonian, with parameters defined in respect to the Bingham plastic approach. This case study evaluated the model performance with the uncalibrated published parameters, reported for 'standard soil' in Julien (1995) [11] [12]. The volumetric concentration of the fluid is adopted at 60%, with yield strength defined through the exponential method with respect to the following coefficients: a = 0.005, b = 7.5 and B = 8 [11] [12]. A widely used formula to estimate the yield stress is the exponential formulation [13] [14] [15]:

$$\tau_y = a \cdot e^{b \cdot C_v} \qquad (1)$$

, where:

τ_y – yield stress,
a, b – Calibration coefficients,
C_v – Volumetric concentration.

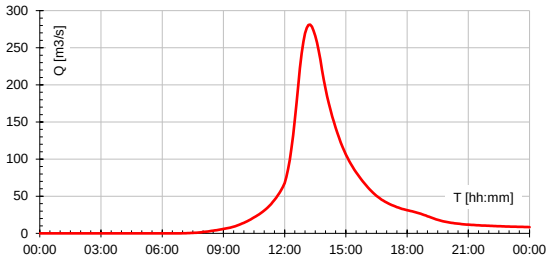

Figure 7. Hydrograph of flood wave for Saska river, with recurrence interval of T = 10 000 years, with max peak Q_{max} = 281.20 m^3/s

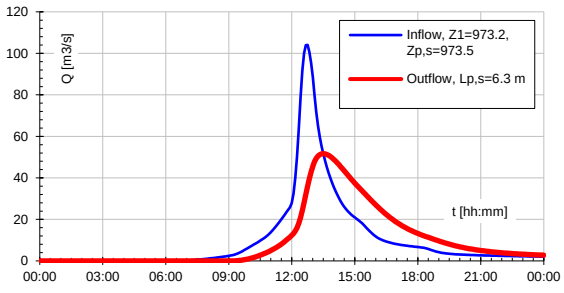

Figure 8. Hydrograph of flood wave for Petrova river, with recurrence interval of T = 10 000 years, inflow and outflow hydrograph

It should be noted that Saska river is completely diverted from the tailing facility location, and its flood wave (Figure 7) is expected to have effect in the riverbed downstream of the TSF Sasa 4, hereinafter it does not contribute to the rainfall – runoff input for any of the scenarios. Its hydrograph is entered as a boundary condition downstream of Sasa 4, and its influence increases the total flood wave effect in the downstream valley, however, it does not have effect on the dams' failure. On the other hand, the tributary of Saska river – river Petrova, enters the reservoir of TSF Sasa 3-2. For evacuation of the expected flood wave (Figure 8), a spillway with tunnel structure is designed in TSF Sasa 3-2 (Figure 9).

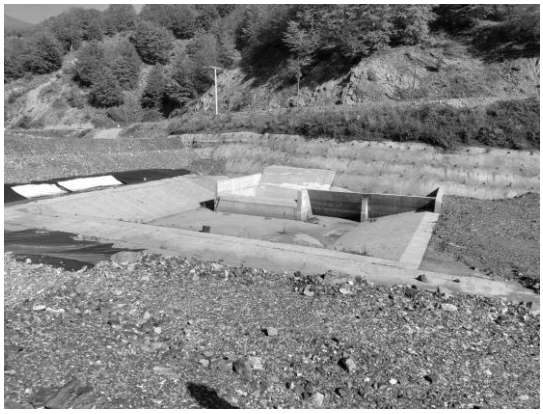

Figure 9. Spillway structure in TSF Sasa 3-2 for evacuation of flood wave from Petrova river

For the overtopping analyses, it is assumed that a trapezoid breach will occur (Figure 10), with top level of breach equal to dam crest elevation, and bottom level equal to the crest elevation of the initial dams respectively. The slopes of the trapezoid breach are assumed as V:H = 1:1, and final bottom width of 60m for TSF Sasa 3-2, and 40m for Sasa 4. The breach formation time is adopted as 24min.

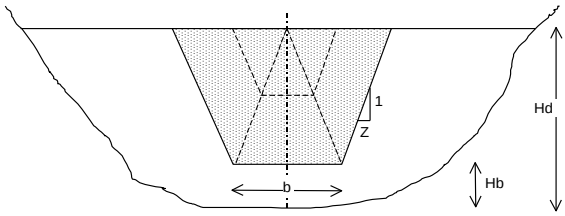

Figure 10. Representative scheme for the mathematical model for overtopping analyses

It is assumed that the failure starts on crest elevation with linear or non-linear progression towards the bottom of the trapezoid breach, where it reaches its final width. Breach flow is calculated with respect to Bernoulli equation for crest spillways.

4. RESULTS AND DISCUSSIONS

The area of interest is located between the TSF Sasa 3-2 as the most upstream point of the model, and the Kalimanci Lake as the most downstream point. Before entering the Kalimanci Lake, Saska river passes through the city of Makedonska Kamenica, and the analyses are greatly focused on determining the flood wave propagation in this zone.

Table 1. Both scenarios with the size of inundation area according to the output results

Scenarios	Inundation area [m^2]	Inundation area [km^2]
Scenario 1	2,110,199	2.11
Scenario 2	**2,137,100**	**2.14**

According to the output results for both scenarios, the second one is more hazardous – just as expected (Table 1). Its flood wave inundates 0.03 km^2 larger area than the first scenario (Figures 13 and 18). The difference between the results paints a picture where the flood wave caused by dam breach is much larger than the one formed by rainfall – runoff. As follows, results are given for both scenarios.

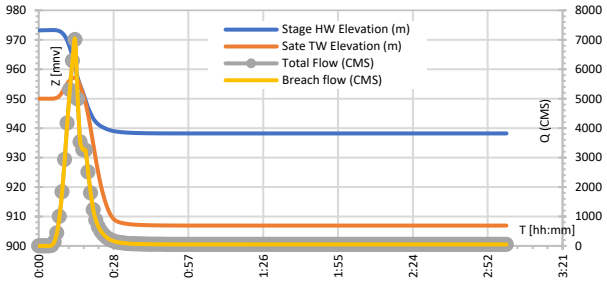

Figure 11. Hydrograph of water level and flood wave in the profile of TSF Sasa 3-2, for scenario 1

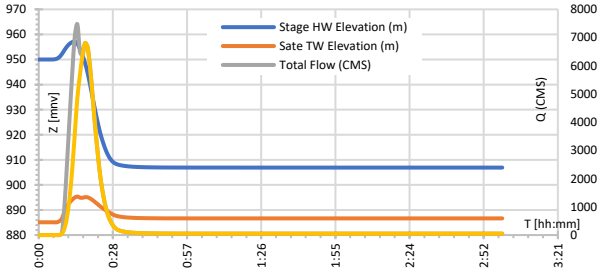

Figure 12. Hydrograph of water level and flood wave in the profile of TSF Sasa 3-2, for scenario 2

For scenario 1 (Figures 11 and 12), the maximal flow expected as breach flow at TSF Sasa 3-2 is Q_{max} = 7006 m^3/s, whereas at TSF Sasa 4 it is Q_{max} = 6652 m^3/s. The total breach flow at TSF Sasa 4 is Q = 7475 m^3/s. As the breach progresses downstream, combined with the flood wave of Petrova river and Saska river, its maximal value just downstream of TSF Sasa 4 is Q = 7609 m^3/s. The time difference between dam breaching of Sasa 3-2 and Sasa 4 is 5min.

The flood wave propagation time is 19min (Table 2), for 12km distance between the most upstream and most downstream profile (Figure 11). The water surface elevation in the city of Makedonska Kamenica reaches 558.0 masl before entering the city, and at the last profile before Kalimanci Lake, it reaches 521.0 masl. The maximal water depth of the flood wave coming through the city, is approximately 9m.

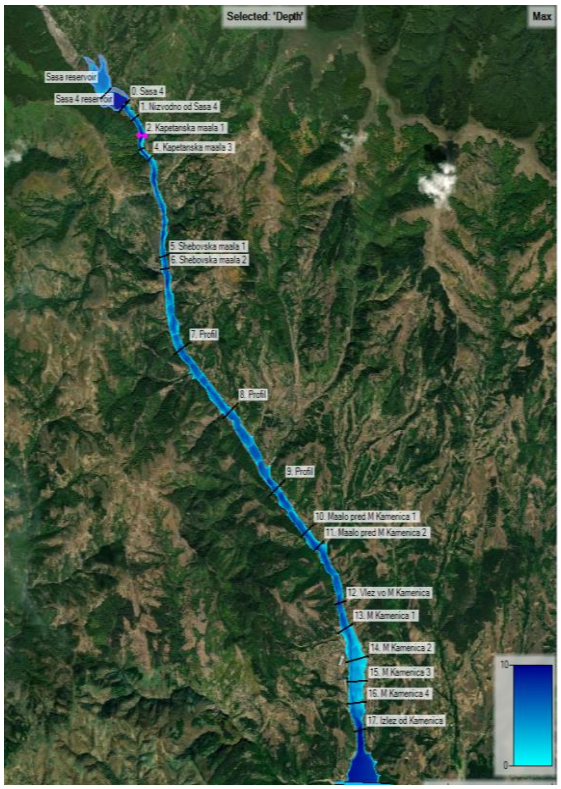

Figure 13. Flood mapping for scenario 1

In order to summarize the results from the conducted analyses, 18 profiles along the downstream riverbed were chosen where hydrodynamic parameters of the flow were observed (Table 2). Profiles located in the city of Makedonska Kamenica are profiles from no. 12 to no. 17.

Table 2. Profiles, maximal flow at each profile, time of flood wave propagation, as well as maximal elevation of water level at right and left riverbank for scenario 1.

Profile	Qmax	t	Elevation (L)	Elevation (R)
	m3/s	hh:mm	m asl	m asl
00=Sasa 4	3273.91	0:15	927.35	928.71
01=Nizvodno od Sasa 4	7609.07	0:15	879.32	880.77
02=Kapetanska maala 1	7472.84	0:15	868.13	868.00
03=Kapetanska maala 2	7278.86	0:15	857.17	857.81
04=Kapetanska maala 3	7382.81	0:16	844.51	844.82

05=Shebovska maala 1	7390.94	0:17	752.06	752.87
06=Shebovska maala 2	7287.58	0:17	743.71	743.66
07=Profil	7216.19	0:19	691.47	691.20
08=Profil	6969.92	0:21	649.08	649.99
09=Profil	6619.12	0:25	611.79	612.08
10=Maalo pred M Kamenica 1	6603.10	0:27	588.11	588.54
11=Maalo pred M Kamenica 2	6566.20	0:27	580.90	581.91
12=Vlez vo M Kamenica	6477.56	0:29	557.95	558.37
13=M Kamenica 1	6389.92	0:30	548.98	549.02
14=M Kamenica 2	6298.10	0:31	535.14	535.54
15=M Kamenica 3	6141.88	0:32	529.03	528.43
16=M Kamenica 4	5986.15	0:33	520.84	521.09
17=Izlez od Kamenica	5676.31	0:34	517.04	516.98

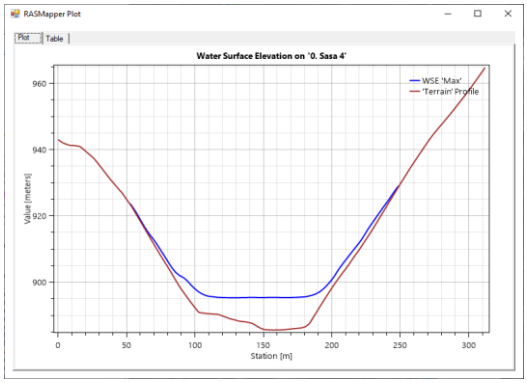

Figure 14. Water surface level at profile 00 – downstream of TSF Sasa 4, for scenario 1

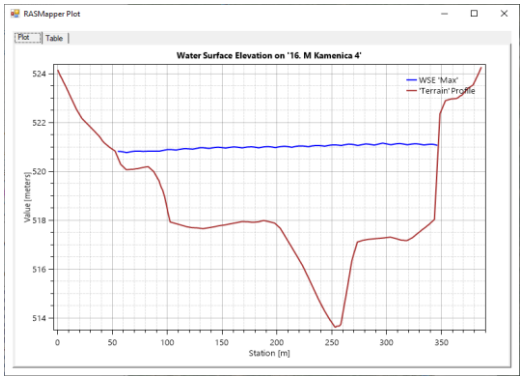

Figure 15. Water surface level at profile 16 – in the city of Makedonska Kamenica, for scenario 1

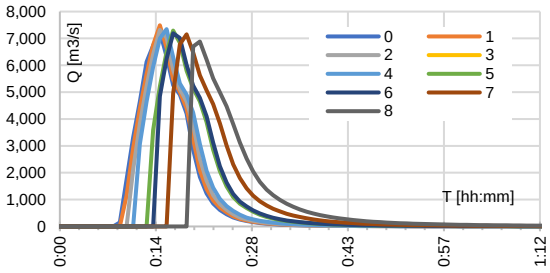

Figure 16. Hydrographs of flood wave propagation for profiles 0 – 9, for scenario 1

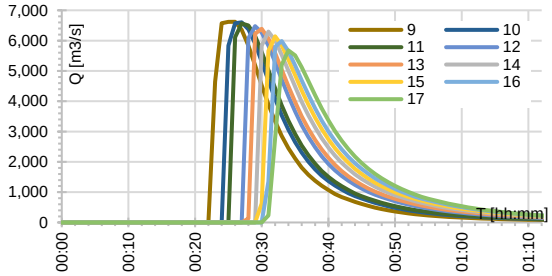

Figure 17. Hydrographs of flood wave propagation for profiles 10 – 17, for scenario 1

For scenario 2 (Figures 19 and 20), the maximal flow expected as breach flow at TSF Sasa 3-2 is Q_{max} = 7458 m^3/s, whereas at TSF Sasa 4 it is Q_{max} = 5684 m^3/s. The total breach flow at TSF Sasa 4 is Q = 7716 m^3/s. As the breach progresses downstream, combined with the flood wave of Petrova reka, its maximal value just downstream of TSF Sasa 4 is Q = 8271 m^3/s. The time difference between dam breaching of Sasa 3-2 and Sasa 4 is 5min.

The flood wave propagation time is 16min (Tab. 2), for 12km distance between the most upstream and most downstream profile (Figure 13). The water surface elevation in the city of Makedonska Kamenica reaches 558.0 masl before entering the city, and at the last profile before Kalimanci Lake, it reaches 521 masl. The maximal water depth of the flood wave coming through the city, is approximately 10m.

Maximal flow velocity during the flood wave is approximately 15 m/s, but not exceeding 10 m/s in the city of Makedonska Kamenica.

Table 3. Profiles, maximal flow at each profile, time of flood wave propagation, as well as maximal elevation of water level at right and left riverbank for scenario 2

Profile	Q_{max}	t	Elevation (L)	Elevation (R)
	m3/s	hh:mm	m asl	m asl
00=Sasa 4	7716.00	9:07	934.75	951.02
01=Nizvodno od Sasa 4	8271.40	9:07	879.82	881.52
02=Kapetanska maala 1	8287.69	9:07	868.54	868.39
03=Kapetanska maala 2	8200.69	9:07	858.03	858.18
04=Kapetanska maala 3	8096.28	9:07	844.63	844.99
05=Shebovska maala 1	8053.94	9:09	752.43	753.06
06=Shebovska maala 2	8110.41	9:09	744.15	744.04
07=Profil	7951.88	9:10	691.83	691.70
08=Profil	7779.89	9:12	649.52	650.51
09=Profil	7457.80	9:14	612.17	612.46
10=Maalo pred M Kamenica 1	7073.62	9:15	588.35	588.81
11=Maalo pred M Kamenica 2	6942.39	9:16	581.08	582.08
12=Vlez vo M Kamenica	6488.97	9:18	558.41	557.93
13=M Kamenica 1	6235.90	9:19	548.99	548.96
14=M Kamenica 2	6073.42	9:20	535.02	535.37

15=M Kamenica 3	5820.36	9:21	528.96	528.34
16=M Kamenica 4	5618.24	9:22	520.79	520.88
17=Izlez od Kamenica	5288.57	9:23	516.88	516.84

Figure 18. Flood mapping for scenario 2

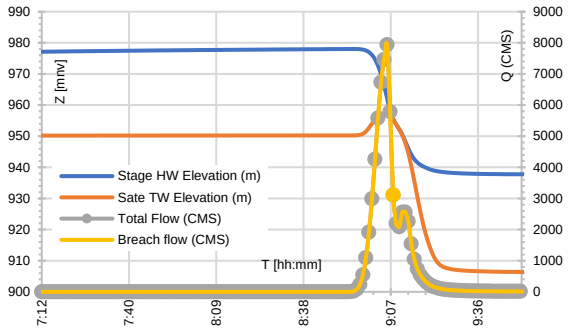

Figure 19. Hydrograph of water level and flood wave in the profile of TSF Sasa 3-2, for scenario 2

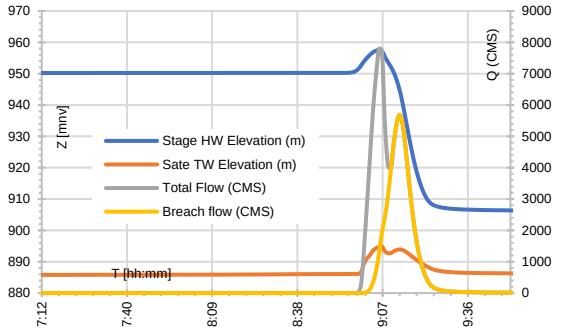

Figure 20. Hydrograph of water level and flood wave in the profile of TSF Sasa 4, for scenario 2

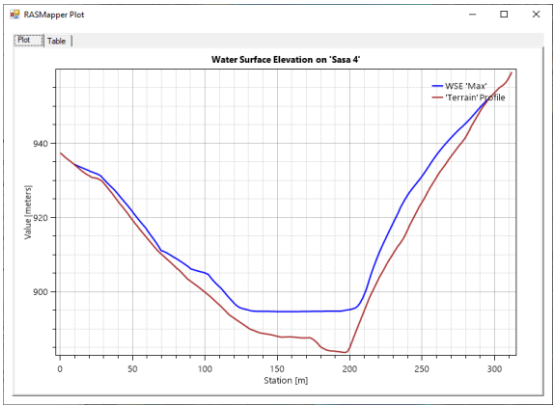

Figure 21. Water surface level at profile 00 – downstream of TSF Sasa 4, for scenario 2

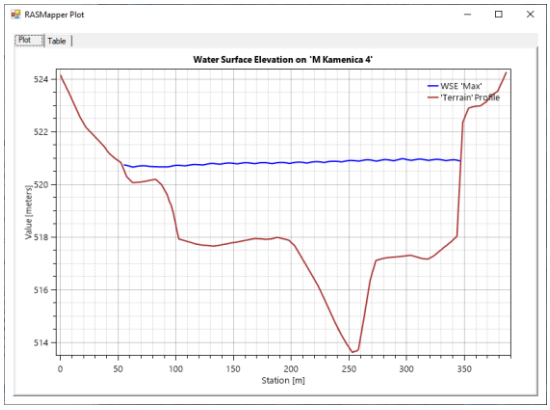

Figure 22. Water surface level at profile 16 – in the city of Makedonska Kamenica, for scenario 2

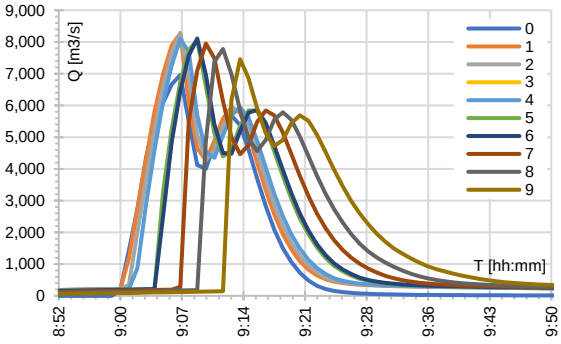

Figure 23. Hydrographs of flood wave propagation for profiles 0 – 9, for scenario 2

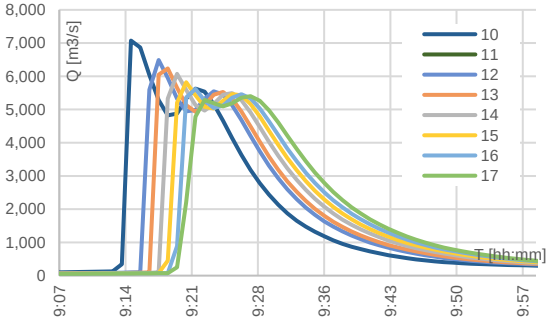

Figure 24. Hydrographs of flood wave propagation for profiles 10 – 17, for scenario 2

CONCLUSIONS

In order to evaluate the effect of breach flow of cascade dam failure, two different models are analyzed by application of plane (2D) HEC RAS software for the cascade system of tailings dams Sasa 3-2 and Sasa 4. Both tailings dams are part of the ore mining facility 'Sasa' located in east RN Macedonia.

Analyses were carried out by application of Lidar topographic maps, designed geometric characteristics of the TSFs and current geometric characteristics of the TSFs according to updated surveying.

Two scenarios were analyzed. First scenario assumes waste lagoons at normal operating levels, and dam failure in static conditions, with rainfall – runoff conditions equal to dry state. The second scenario assumes dam failure caused by overtopping, with flood wave formed with rainfall – runoff from the upstream basin of Petrova and Saska river with probability of reccurrence of 1 in 10 000 years.

For scenario 1, the maximal flow expected as breach flow at TSF Sasa 3-2 is Q_{max} = 7006 m^3/s, whereas at TSF Sasa 4 it is Q_{max} = 6652 m^3/s. The total breach flow at TSF Sasa 4 is Q = 7475 m^3/s. As the breach progresses downstream, combined with the flood wave of Petrova river and Saska river, its maximal value just downstream of TSF Sasa 4 is Q = 7609 m^3/s. The time difference between dam breaching of Sasa 3-2 and Sasa 4 is 5min.

For scenario 2, the maximal flow expected as breach flow at TSF Sasa 3-2 is Q_{max} = 7458 m^3/s, whereas at TSF Sasa 4 it is Q_{max} = 5684 m^3/s. The total breach flow at TSF Sasa 4 is Q = 7716 m^3/s. As the breach progresses downstream, combined with the flood wave of Petrova reka, its maximal value just downstream of TSF Sasa 4 is Q = 8271 m^3/s. The time difference between dam breaching of Sasa 3-2 and Sasa 4 is 5min.

It can be concluded that the effect of the flood wave caused by rainfall – runoff coming from the upstream basin of Petrova and Saska river is very minor compared to the flood wave caused by the cascade dams failure.

The alarming time between the initial breaching of the upstream Sasa 3-2 dam, and the arrival time of the flood wave in the city of Makedonska Kamenica, is very short – 15min for the second scenario which is the more hazardous one compared to scenario 1.

REFERENCES

[1] Tanchev, Lj. (2014), 'Dams and appurtenant hydraulic structures', 2nd edition, Taylor & Francis Group, London, UK.

[2] National Environment Protection Council (South Australia), Act 1995.

[3] Davies, M. P., Martin, T.E. (2000), 'Upstream constructed tailings dams – a review of the basics', Tailings and Mine Waste 00, Colorado, USA, A.A. Balkema, Rotterdam, pp. 3-15.

[4] Vrhovnik, P., Dolenec, T., Serafimovski, T., Dolenec, M., Rogan S., Nastja (2013), 'The occurence of heavy metals and metalloids in surficial lake sediments before and after tailings dam failure', Polish Journal of Environmental Studies vol. 22 no. 2 (2013) pp. 1525 – 1538.

[5] Diehl, P. World Information Service on Energy (WISE) Uranium project (online). Available from: https://www.wise-uranium.org/mdaf.html

[6] DIPKO Skopje (2022), 'Elaborate for the effect of flood wave propagation caused by dam colapse of tailings dams in mine Sasa, M. Kamenica', Petkovski Ljupcho (designer in charge).

[7] Martin, V., Adria, D., Wong, H. (2022), 'Inundation modelling of non – newtonian tailings dam breach outflows', 27th Congress of large dams, ICOLD, Marseille, June 2022.

[8] Bornchein A. (2009), 'A simple method to estimate inundation due to dam break', 2nd International conference on long term behaviour of dams, 12-13 October, Graz, Austria, ISBN 978-3-85125-070-2.

[9] Froehlich D.C. (1995), 'Peak outflow from breached embankment dam', Water Resources Planning and Management (ASCE), Vol.121 No.1, p.90-97.

[10] Hagen D.C., Webby M.G., Froehlich D.C. (1996), Discussion on "Peak outflow from breached embankment dam", Water Resources Planning and Management (ASCE), Vol.122 No.4, p.314-319.

[11] Julien, P.Y. (1995), Erosion and Sedimentation; Cambridge University Press: Cambridge, UK, p. 280.

[12] HEC. HEC-RAS 2D User's Manual v6.1. 2021

[13] Chien, N., and Ma, H. (1958), Properties of slurry flow. J. Sediment Res. 3(3), Beijing, China (in Chinese).

[14] Dai, Z., Huang, Y., Cheng, H., and Xu, Q. (2014), 3D numerical modeling using smoothed particle hydrodynamics of flow-like landslide propagation triggered by the 2008 Wenchuan earthquake. Eng. Geol. 180, 21–33.

[15] O'Brien, J.S., and Julien, P.Y (1988), Physical properties and mechanics of Hyperconcentrated sediment flows, Proc. ASCE Hyd. Deiv. Spec. Conf. Delineation of Landslides, Flash Flood, and Debris Flow Hazards, Logan Utah, June 1984, 260–279.

TRANSVERSE MERCATOR PROJECTION FOR THE TERRITORY OF MACEDONIA

Zlatko Srbinoski
PhD, Full Professor
University 'Ss. Cyril and Methodius'
Faculty of Civil Engineering – Skopje
N. Macedonia
srbinoski@gf.ukim.edu.mk

Zlatko Bogdanovski
PhD, Associate Professor
University 'Ss. Cyril and Methodius'
Faculty of Civil Engineering – Skopje
N. Macedonia
bogdanovski@gf.ukim.edu.mk

Filip Kasapovski
PhD, Assistant Professor
University 'Ss. Cyril and Methodius'
Faculty of Civil Engineering – Skopje
N. Macedonia
kasapovski@gf.ukim.edu.mk

Tome Gegovski
MSc, Teaching Assistant
University 'Ss. Cyril and Methodius'
Faculty of Civil Engineering – Skopje
N. Macedonia
gegovski@gf.ukim.edu.mk

Filip Petrovski
MSc, Teaching Assistant
University 'Ss. Cyril and Methodius'
Faculty of Civil Engineering – Skopje
N. Macedonia
petrovski@gf.ukim.edu.mk

In this work are given characteristics of Transverse Mercator projection and possibilities for their application like a state's cartographic projection. Then, there are defined the basic elements of projection applicant on territory of Republic of Macedonia. In the end, there are presented some advantages of TM projection beyond Gauss-Kruger's projection like an existing state's cartographic projection.

Keywords: states cartographic projection, Transverse Mercator projection.

1. INTRODUCTION

A list of advantages that allow the conformal representation of the Earth's ellipsoid around the circumference of the cylinder, were first discovered by the Dutch cartographer , Gerhard Kremer Mercator in the 16th century.

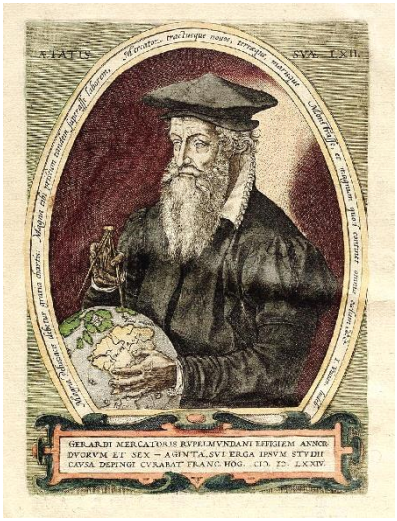

Figure 1. Gerhard Kremer Mercator – creator of the normal conformal cylindrical cartographic projection

He applied the normal conformal cylindrical projection for the creation of the World's Map for the first time in 1569. This map has been considered as the biggest achievement in the history of carthography and the projection was named Mercator's projection. Some time later, the applicability of transverse cylindrical projections for mapping parts of Earth's surface that have meridian extension was used. More distinguished surveyors and cartographers, such as: Gauss, Cassini, Lambert, Schreiber,

Hristov and others worked on developing mathematical expressions for transverse cylindrical projections.

In honor of the great cartographer Mercator, the transverse conformal cylindrical projection is called Transverse Mercator projection. Transverse Mercator projection (together with Lambert conformal conic projection and Stereographic projection) is among the projections that are most often used for geodetic purposes. Over time, the name "geodetic projections" was established for the projections. The basic characteristics are:

- geodetic projections are used to calculate Cartesian coordinates in the plane for points from the geodetic base network, that are set for the needs of surveying a certain territory;
- geodetic projections are used for creation of large and medium scaled topographic plans and topographic maps;
- original surface in these projections is the surface of the reference ellipsoid, which was chosen as the basis of the survey, etc.

Geodetic projections were especially developed in the second half of the 19th and the beginning of the 20th century, with the intensification of the work of the state's survey in several countries. At the time, Cassini-Soldner equidistant transverse cylindrical projection was especially used. In modern times, the most widely used projection is the Transverse Mercator projection which is accepted as the state cartographic projection in most countries in the world.

2. BASIC CHARACTERISTICS OF THE TRANSVERSE MERCATOR PROJECTION

In the Transverse Mercator projection, the ellipsoid is mapped onto elliptical cylinders, where each cylinder touches the ellipsoid in the middle meridian of the territory that is being mapped.

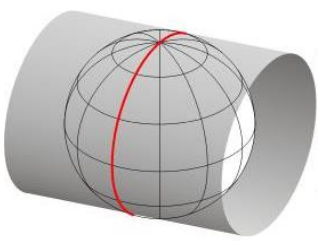

Figure 2. Tangent cylinder of Earth's ellipsoid

According to the projection's theory, the mapping is done under the following conditions:

- Conformal projection – with no angle deformations;
- The mean meridian should be mapped as straight line and its projection should have an equal or constant ratio.

According to the characteristics of the projection, in each zone, only the equator and the central meridian are mapped in the plane as straight lines. The other meridians and parallels are mapped in the form of curved lines, symmetrical in relation to the equator and the central meridian.

The Cartesian coordinate system in the Transverse Mercator projection can be set arbitrarily, where the projection of the central meridian defines the X-axis and the projection of the equator defines the Y-axis of the system. The width of the mapped territory in the coordinate system of the Transverse Mercator projection is defined with the maximum allowed linear deformations.

From what has been said so far, it can be concluded that Transverse Mercator projection is basically identical to the Gauss-Kruger projection. The difference between the projections consists of several things about the Transverse Mercator projection:

- Possibility in selection of the mean meridian for the territory that needs to be mapped;
- Possibilty in selection of territory's width that needs to be mapped in one coordinate system;
- Possibilty for selection of arbitrary module of the linear deformations, whose value does not have to be fixed at -10 cm/km, which makes it possible to obtain better spatial data when mapping the territories with width smaller than 254 km.

Practically, the Gauss-Kruger projection represents a variant of the Transveral Mercator projection with strictly defined rules that enable its universal appllication. However, due to its inflexibility, it is not suitable for mapping small territories, assymetrical in relation to the mean meridian, as is the case with the Republic of Macedonia.

The identical mathematical equations, makes the calculation of the basic dimensions in the Transverse Mercator projection to be made with the known mathematical expressions from the Gauss-Kriger projection.

1. The calculation of the Cartesian coordinates (X, Y) in the plane, for the points on the ellipsoid that are defined by the geographic coordinates φ, λ is done with the following equations:

$$X = \overline{X} + (X_1)\ l^2 + (X_2)\ l^4 + (X_3)\ l^6 \qquad (1)$$

$$Y = (Y_1)\ l + (Y_2)\ l^3 + (Y_3)\ l^5 \qquad (2)$$

$\overline{X}$ - length of meridian arc,
l – difference of longitudes l = λ - λ_o,
(X_1) - (X_3) i (Y_1) - (Y_3) - coefficients.

2. Calculation of latitude and longitude (φ, λ) on the ellipsoid, for points that are defined with Cartesian coordinates (X, Y) in the plane, is done with the following expressions:

$$\varphi = \varphi' + (\varphi_1)\ \overline{Y}^2 + (\varphi_2)\ \overline{Y}^4 + (\varphi_3)\ \overline{Y}^6 \qquad (3)$$

$$l = (l_1)\ \overline{Y} + (l_2)\ \overline{Y}^3 + (l_3)\ \overline{Y}^5 \qquad (4)$$

$\overline{Y}$ - ordinate of a point in relation with the central meridian,
(φ_1) - (φ_3) i (l_1) - (l_3) - coefficients,
φ' – latitude that is obtained in an iterative procedure.

3. Linear deformations in transverse cylindrical projection are calculated with the following expression:

$$\Delta d = d - s = s\frac{\overline{Y}_1^2 + 4\overline{Y}_m^2 + \overline{Y}_2^2}{12R_m^2} \qquad (5)$$

d – length of distance in the projection,
s – length of distance on the ellipsoid,
Δd – linear deformation,
$\overline{Y}_1$, $\overline{Y}_2$ - ordinates of endpoints of the line,
$\overline{Y}_m$ - mean ordinate,
R_m – mean curvature radius.

4. The convergence of the meridians at a given point of the projection can be calculated based on the given geographical or Cartesian coordinates for the point.

With known values of geographic coordinates (φ, λ) of a given point in the projection, the convergence of the meridians is calculated with the following expression:

$$c = l\sin\varphi + (c_1)\ l^3 + (c_2)\ l^5 \qquad (6)$$

And if the rectangular coordinates (Y, X) of the point in the projection are known, the convergence of the meridians is calculated with the following expression:

$$c = (c_3)\ \overline{Y} + (c_4)\ \overline{Y}^3 + (c_5)\ \overline{Y}^5 \qquad (7)$$

$\overline{Y}$ - ordinate of a point related to the central meridian,
(c_1) - (c_5) – coefficients,
l – difference of longitudes l = λ - λ_o,

3. ELEMENTS FOR DEFINING THE TRANSVERSE MERCATOR PROJECTION FOR THE TERRITORY OF MACEDONIA

When applying the Transverse Mercator projection, it is necessary to determine the central meridian of the area that is being mapped. The geographic longitude of the central meridian for the territory of our country can be obtained as the arithmetic mean of the geographic longitudes of its extreme points – the easternmost and the westernmost. The easternmost point in the Republic of Macedonia is the border stone num. 47 called Chengino Kale, while the westernmost point is the border stone E16/VIII called Kestenjar. The coordinates of those points are obtained from topographic map TK 25 and those values are:

Table 1. Extreme points of the state's territory

	φ	λ
Chengino Kale	41° 42' 32"	23° 02' 23"
Kestenjar	41° 31' 03"	20° 27' 32"

Arithmetic mean of geographic longitudes is:

$$\lambda_{sr} = \frac{\lambda_{\min} + \lambda_{\max}}{2} = 21^o 44'57''.5 \qquad (8)$$

In that case, for the mean meridian can be chosen the meridian that have geographic longitudal value of **λ_o = 21° 45'** that is only 2.5" (cca 58 m) far from the ideal mean of the territory of Macedonia.

The Cartesian coordinate system (Y, X), in the Transverse Mercator projection for the Macedonia, is defined by the projections of the equator and the central meridian. Moreover, the projection of the meridian λ_o = 21° 45' defines the X-axis, while the projection of the equator defines the Y-axis of the Cartesian coordinate system.

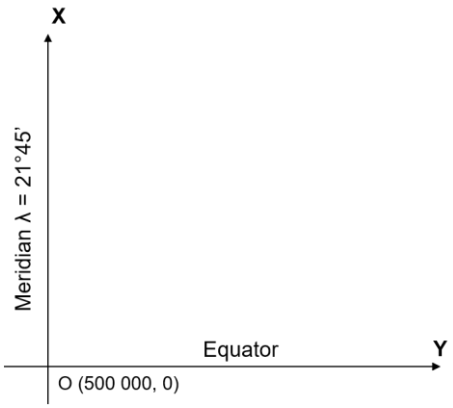

Figure 3. Coordinate system of the Transverse Mercator projection

Taking into account the dimensions of the territory of Macedonia, it is possible to calculate the maximum linear deformations of the projection that will be obtained at easternmost and westernmost points. If the length of the geodetic line is taken as the length of the arc of the parallel between the mean meridian (λ_o = 21° 45') and the meridian of the eastern-most and westernmost point (which is about 107.7 km), therefore for the assumed radius of R = 6375 km, the maximum linear deformation is:

$$\Delta d_{max} = 14.3 \text{ cm/km}$$

The accuracy of the projection can be increased by introducing a negative linear deformation (-7 cm/km) on the mean meridian, by introducing the secant cylinder. With the help of the secant cylinder, in the area of 106.67 km east and west of the central meridian, the linear deformations will be less than **± 7 cm/km**. Outside of this area, only a small part of the country's territory will remain where the linear deformations would not be bigger than **+7.3 cm/km**. The inclusion of the linear deformation with value of -7 cm/km is made by multiplying of the Cartesian coordinates ($\overline{Y}$, $\overline{X}$) by the linear module:

$$m = 0.99993$$

In that way, the modified Cartesian coordinates (Y, X) are calculated with the following expressions:

$$Y = \overline{Y} \cdot 0.99993 + 500000 \ m$$
$$X = \overline{X} \cdot 0.99993 \quad (9)$$

From the expression, it can be seen that, in addition to the reduction, a translational displacement of the coordinate system by 500000 m to the west is performed, thus avoiding negative Y-coordinates (Figure 3).

3.1 LINEAR DEFORMATIONS AND ISOCOLS IN THE TRANSVERSE MERCATOR PROJECTION

Isocols in the Transverse Mercator projection are straight lines that are parallel with the projection of the central meridian that are defined by adequate ordinates $\overline{Y}$.

Isocols for the territory of Macedonia are shown in Table 2.

Table 2. Isocols of the Transverse Mercator projection of Macedonia

Deformations (cm/km)	Isocols $\overline{Y}$ (km)
0	0
1	± 28.5
2	± 40.3
3	± 49.4
4	± 57.0
5	± 63.8
6	± 69.8
7	± 75.4
8	± 80.6
9	± 85.5
10	± 90.2
11	± 94.6
12	± 98.8
13	± 102.8
14	± 106.7

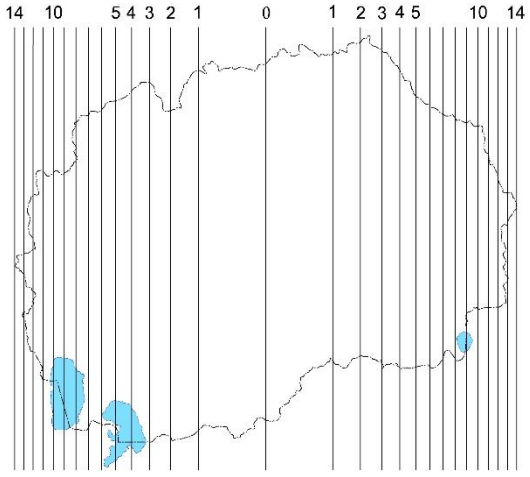

Figure 4. Isocols in the TM projection

After inclusion of the negative linear deformation on the mean meridian of -7 cm/km and

reduction of the Cartesian coordinates, the isocols in the TM projection have values in the interval from -7 cm/km to +7.3 cm/km.

Table 3. Isocols of the Transverse Mercator projection after the reduction

Deformations (cm/km)	Isocols $\bar{Y}$ (km)
-7	0
-6	± 28.5
-5	± 40.3
-4	± 49.4
-3	± 57.0
-2	± 63.8
-1	± 69.8
0	± 75.4
1	± 80.6
2	± 85.5
3	± 90.2
4	± 94.6
5	± 98.8
6	± 102.8
7	± 106.7

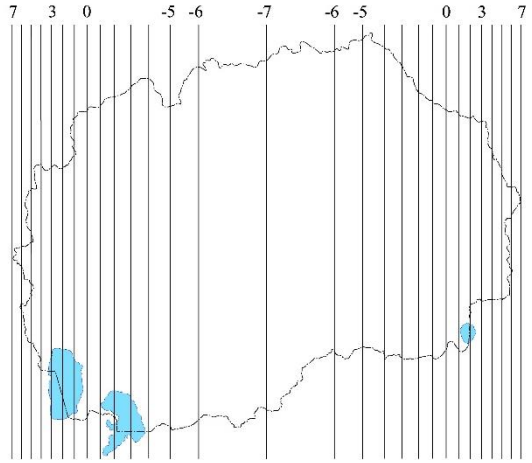

Figure 5. Isocols in TM projection after the reduction

The average linear deformation on the whole territory of Macedonia that is in the Transverse Mercator projection:

Θ = 3.67 cm/km

After the reduction of the Cartesian coordinates and the introduction of a secant-variant of the TM projection, the average linear deformation gets a value:

Θ = 4.32 cm/km

3.2 CONVERGENCE OF MERIDIANS

The convergence of the meridian, identically as for the Gauss-Kruger projection, is a quantity that depends of the distance from the meridian of a given point in relation to the central meridian in the projection. Because of the fact that in the Transverse Mercator projection, the X-axis of the coordinate system is identical to the meridian that is near the center of the state's territory, the meridian convergence has almost identical values on both extreme points (easternmost and westernmost) for the territory of Macedonia.

The maximum value of meridian convergence for the easternmost point in the country is:

$$c = +0^{o}\ 51'\ 29.43''$$

4. CONCLUSIONS

On the basis of what has been said above, the basic properties of the Transverse Mercator projection for Macedonia can be sublimated:

- Transverse Mercator projection has the same mathematical expressions as Gauss-Kruger projection;
- The coordinate system of the projection is defined by the projections of the equator and the mean meridian with geographic longitude of $\lambda_o = 21^o\ 45'$;
- Isocols are parallel straight lines, symmetrical in relation to the projection of the central meridian;
- The maximum linear deformation value in the Transverse Mercator projection for Macedonia is *14.3 cm/km;*
- Average linear deformation for the whole country has a value of *3.67 cm/km;*
- For better spatial data quality, the Cartesian coordinates are modulated with constant linear module which has value of m = 0.99993. That means introducing negative linear deformation on the central meridian with the value of -7 cm/km. In that way, the maximum value of linear deformations is being reduced and has a value of *7.3 cm/km;*
- The meridian convergence has a max. value in the easternmost point in the country and its value is: $c_i = +0^o\ 51'\ 29.43''$;
- The distribution of linear deformations for Macedonia is symmetrical and in relation

to the central meridian which geographic longitude is $\lambda = 21^{o}\ 45'$;

- The projections has detailed mathematical expressions that allow calculation of the geodetic tasks in the plane of the projection;
- More than 80% of the European countries are using a variant of the Transverse Mercator projection for the purpose of state surveying and official cartography.

REFERENCES

[1] Borčić B. (1955), Mathematical mapping (cartographic projections), Technical book, Zagreb.

[2] Jovanovic V. (1983), Mathematical Cartography, VGI, Belgrade.

[3] Ribarovski R (1994), Introduction in advanced geodesy, Faculty of Civil Engineering - Skopje.

[4] Srbinoski Z. (2001), Enclosure to research on defining a new state cartographic projection, Doctoral dissertation, University "St. Cyril and Methodius ", Skopje.

[5] Srbinoski Z. (2009), Mathematical Cartography, Faculty of Civil Engineering - Skopje.

[6] Srbinoski Z. (2019), Study on the selection of a new state cartographic projection, Agency for Real Estate Cadastre, Skopje.